Ministry of Science, Research and Technology

Damghan University

Astronomical Society of Iran

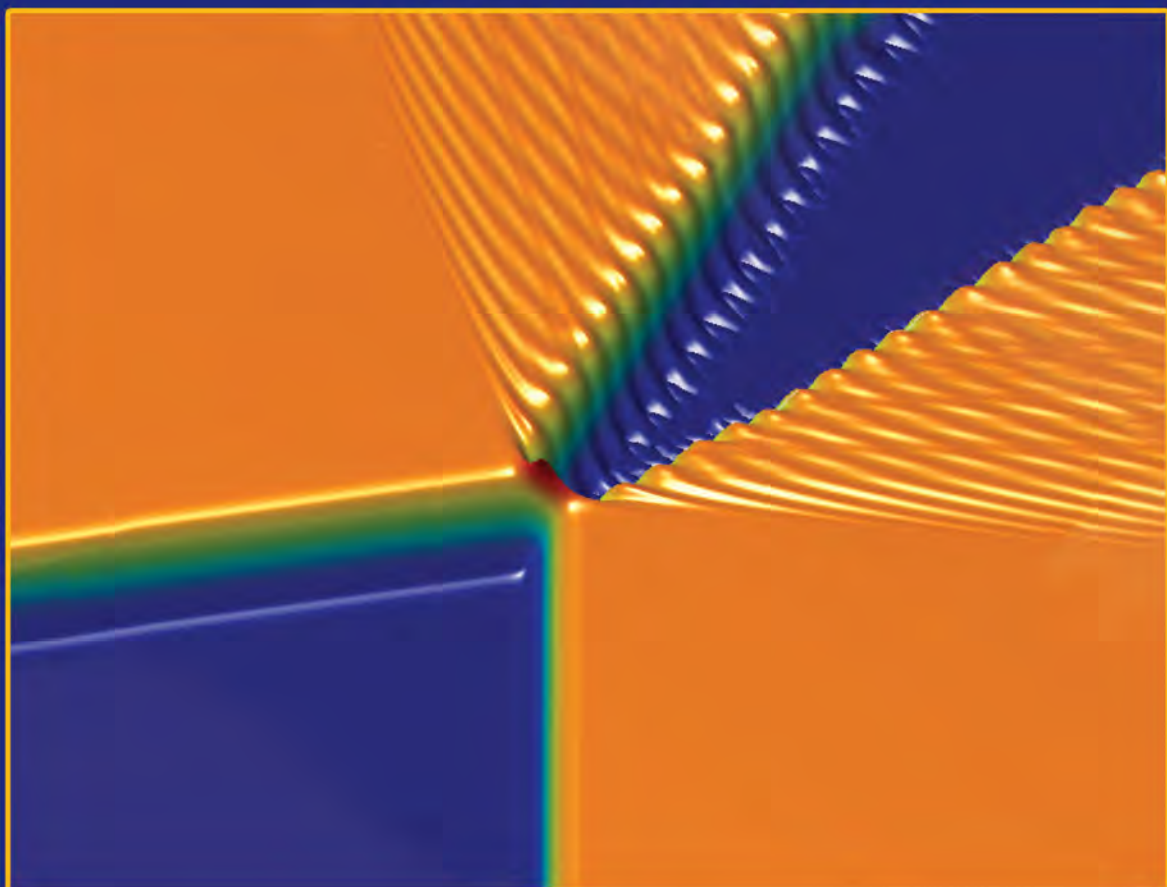# IJAA

Iranian Journal of Astronomy and Astrophysics

For any arbitrary complex Kink-anti-kink collision, depending on initial phases, it leads to different collision fates

(M. Mohammadi et al, IJAA, 4, 1, 2017)

Iranian Journal of Astronomy and Astrophysics (IJAA)

Vol. 4, No. 1, 2017

This journal is the collaborative results of Damghan University and the Astronomical Society of Iran, and it is published twice per year.

Editorial Board

Contents

Noether Symmetry in f(T) Theory at the anisotropic universe

A. Aghamohammadi

Sanandaj Branch, Islamic Azad University, Sanandaj, Iran; email:a.aqamohamadi@gmail.com;
a.aghamohamadi@iausdj.ac.ir

Abstract. As it is well known, symmetry plays a crucial role in the theoretical physics. On other hand, the Noether symmetry is a useful procedure to select models motivated at a fundamental level, and to discover the exact solution to the given lagrangian. In this work, Noether symmetry in f(T) theory on a spatially homogeneous and anisotropic Bianchi type I universe is considered. We discuss the Lagrangian formalism of f(T) theory in anisotropic universe. The point-like Lagrangian is clearly constructed.The explicit form of f(T) theory and the corresponding exact solution are found by requirement of Noether symmetry and Noether charge. A power-law f(T), the same as the FRW universe, can satisfy the required Noether symmetry in the anisotropic universe with power- law scale factor. It is regarded that positive expansion is satisfied by a constrain between parameters.

Keywords: Noether symmetry, anisotropic Bianchi type I universe, modified theories of gravity, $f(T)$ gravity

1 Introduction

In this work, our aim is to study a Noether symmetry of scalar torsion gravity in anisotropic univers.

Recently, some astrophysical observations have shown that the Universe is undergoing an accelerated phase era. To justify this unexpected result, scientists have proposed some different models such as, scalar field models [1, 2, 3, 4] and modify theories of gravity [5, 6, 7, 8]. For the latter proposal, one can deal with telleparallel equivalent of general relativity [9, 10, 11, 12], in which the field equations are second order [13]. In addition, in this scenario the Levi-Civita connections are replaced by Weitzenböck connection where it has no curvature but only torsion [14].

A Bianchi type I (BI) universe, being the straightforward generalization of the flat FRW universe, is of interest because it is one of the simplest models of a non-isotropic universe exhibiting a homogeneity and spatial flatness. In this case, unlike the FRW universe which has the same scale factor for three spatial directions, a BI universe has a different scale factor for each direction. This fact introduces a non-isotropy to the system. The possible effects of anisotropy in the early universe have been investigated with BI models from different points of view [25, 26, 27, 28]. Some people [29, 30] have constructed cosmological models by using anisotropic fluid and BI universe. Recently, this model has been studied in the presence of binary mixture of the perfect fluid and the DE [31]. Further, there are some exact solutions for BI models in f (T) gravity [32]

The outline of this work is as follows. In the next section, a brief review of the general formulation of the field equations in a BI metric and $f(T)$ garavity are discussed, Sec. 3 is concerned with Lagrangian formalism of f(T) theory in anisotropic universe. Sec. 4, is related to Noether symmetry in f(T) theory in anisotropic universe. We summarize our results in last section.

2   General Framework

The telleparallel theory of gravity is defined in the Weitzenböck's space-time, with torsion and zero local Riemann tensor, in which we are working in a non-Riemannian manifold. The dynamics of the metric were determined using the scalar torsion T . The fundamental quantity in teleparallel theory is the vierbein (tetrad) basis $e^i{}_\mu$. This basis is an orthogonal, coordinate free basis defined by the following equation

$$g_{\mu\nu} = \eta_{ij} e^i{}_\mu e^j{}_\nu, \tag{1}$$

where $\eta_{ij} = diag[1, -1, -1, -1]$ and $e_i{}^\mu e^i{}_\nu = \delta^\mu_\nu$ or $e_i{}^\mu e^j{}_\mu = \delta^j_i$. and the matrix $e^a{}_\mu$ are called tetrads that indicate the dynamic fields of the theory, where Latin i, j are indices running over $0, 1, 2, 3$ for the tangent space of the manifold, and Greek μ, ν are the coordinate indices on the manifold, also running over $0, 1, 2, 3$. In the framework of $f(T)$ theory, Lagrangian density is extended from the torsion scalar T to a general function $f(T)$, similar to what happened in $f(R)$ theories. The action S of modified telleparallel gravity is given by [33, 34]

$$I = \int \mathrm{d}^4 x |e| f(T) + L_m\Big], \tag{2}$$

where for convenience, we use the units $2k^2 = 16\pi G = 1$, $|e| = det(e^i_\mu) = \sqrt{-g}$ and e^i_μ forms the tangent vector of the manifold, which is used as a dynamical object in telleparallel gravity, L_M is the Lagrangian of matter. The components of the tensor torsion and the contorsion are defined respectively as

$$T^\rho{}_{\mu\nu} \equiv e_l{}^\rho \left(\partial_\mu e^l{}_\nu - \partial_\nu e^l{}_\mu \right) , \tag{3}$$

$$K^{\mu\nu}{}_\rho \equiv -\frac{1}{2} \left(T^{\mu\nu}{}_\rho - T^{\nu\mu}{}_\rho - T_\rho{}^{\mu\nu} \right) . \tag{4}$$

It was defined a new tensor $S_\rho{}^{\mu\nu}$ to obtain the scalar equivalent to the curvature scalar of general relativity i.e. Ricci scalar, that is as

$$S_\rho{}^{\mu\nu} \equiv \frac{1}{2} \left(K^{\mu\nu}{}_\rho + \delta^\mu_\rho T^{\alpha\nu}{}_\alpha - \delta^\nu_\rho T^{\alpha\mu}{}_\alpha \right). \tag{5}$$

Hence, the torsion scalar is defined by the following contraction

$$T \equiv S_\rho{}^{\mu\nu} T^\rho{}_{\mu\nu}. \tag{6}$$

By using the components (Eq.4,Eq.5), the torsion scaler (Eq. 6) gives

$$T \equiv -6H^2 + 2\sigma^2. \tag{7}$$

Bianchi cosmologies are spatially homogeneous but not necessarily isotropic. Here, we will consider BI cosmology. The metric of this model is given by

$$ds^2 = dt^2 - A^2(t)dx^2 - B^2(t)dy^2 - C^2(t)dz^2, \tag{8}$$

where the metric functions, A, B, C, are merely functions of time, t and related to scale factor by $a = (ABC)^{\frac{1}{3}}$. In this work for convenience, we assume $B = C = A^m$, where m is a constant. It is defined the shear tensor as describes the rate of distortion of the matter flow, that in a comoving coordinate system, from the metric (Eq.8), the components of the average Hubble parameter and the shear tensor are given by [38]

$$
\begin{aligned}
H &= \frac{1}{3}(\frac{\dot{A}}{B} + \frac{\dot{B}}{B} + \frac{\dot{C}}{C}), \\
\sigma^2 &= \frac{1}{2}[(\frac{\dot{A}}{A})^2 + (\frac{\dot{B}}{B})^2 + (\frac{\dot{C}}{C})^2] - \frac{3}{2}H^2.
\end{aligned}
\tag{9}
$$

3 Lagrangian Formalism of f(T) Theory in Anisotropic Universe

In this section, we discuss the Lagrangian formalism of f(T) theory in anisotropic universe .In the study of Noether symmetry,It is clear that the point-like Lagrangian plays a crucial role. From the action f(T) (Eq.2), and following [36, 35, 37], to derive the cosmological equations in the Bianchi I metric, (BIm), one can define a canonical Lagrangian $\mathcal{L} = \mathcal{L}(A, \dot{A}, T, \dot{T})$, whereas $Q = a, T$ is the configuration space, and $\mathcal{T}Q = [A, \dot{A}, T, \dot{T}]$ is the related tangent bundle on which L is defined. The factor A(t) and the torsion scalar T (t) are taken as independent dynamical variables. One can use the method of Lagrange multipliers to set T as a constraint of the dynamics (Eq. 6). Selecting the suitable Lagrange multiplier and integrating by parts, the Lagrangian $\mathcal{L}$ becomes canonical [36, 35] theory which is given by

$$
I = 2\pi^2 \int \mathrm{d}t ABC\big[f(T) - \lambda(T + 6H^2 - 2\sigma^2) - \frac{\rho_{m0}}{ABC}\big],
\tag{10}
$$

where λ is a Lagrange multiplier. The variation with respect to T of this action gives

$$
\lambda = f_T.
\tag{11}
$$

So, the action (10) can be rewritten as

$$
I = 2\pi^2 \int \mathrm{d}t ABC\big[f(T) - f_T(T + 6H^2 - 2\sigma^2) - \frac{\rho_{m0}}{ABC}\big],
\tag{12}
$$

and then the point-like Lagrangian reads (up to a constant factor $2\pi^2$)gives

$$
\mathcal{L}(A, \dot{A}, T, \dot{T}) = A^{1+2m}\big[f(T) - f_T(T + 6H^2 - 2\sigma^2)\big] - \rho_{m0},
\tag{13}
$$

where using from assume $B = C, a^3 = A^{1+2m}$. Writing (13) with respect (9) yield

$$
\mathcal{L}(A, \dot{A}, T, \dot{T}) = A^{1+2m}\big[f - f_T T + 2f_T(\frac{\dot{A}}{A})^2 c_0\big] - \rho_{m0},
\tag{14}
$$

where $c_0 = 1/3(2m+1) - (1+2m)^2/3 - m^2)$, and setting $m = 1$ reduce equation (Eq.14) to the same form of lagrangian equation in isotropic univerce, i.e. FRW metric [37], as well, the equation lagrangian form in the FRW metric constrained $c_0 \neq 0, -2/7$. As it is explicit for a dynamical system, the Euler-Lagrange equation is written

$$
\frac{d}{dt}(\frac{\partial \mathcal{L}}{\partial \dot{q_i}}) = \frac{\partial \mathcal{L}}{\partial q_i},
\tag{15}
$$

where q_i are A, T in this case. Substituting Eq. (14) into the Euler-Lagrange equation (Eq.15), we get the following equations with respect T, A respectively

$$A^{1+2m} f_{TT} \big[-T + 2(\frac{\dot{A}}{A})^2 c_0 \big] = 0, \qquad (16)$$

$$4 f_{TT} \dot{T} \dot{A} + 4 f_T \ddot{A} c_0 + 2 f_T (\frac{\dot{A}}{A})^2 (2m - 1) c_0 - (1 + 2m)(f - f_T T) = 0. \qquad (17)$$

From Eq. (16), it is easy to find that if $f_{TT} \neq 0$

$$T = 2(\frac{\dot{A}}{A})^2 c_0 = -6H^2 + 2\sigma^2. \qquad (18)$$

That, setting $m = 1$ reduce equation (18) to the same form of torsion scaler from FRW metric, [37] . In addition, the relation (7) is recovered. Mainly, this is the Euler constraint of the dynamics. Substituting Eq. (18) into Eq. (17), we get

$$8 f_{TT} c_0^2 \frac{\dot{A}}{A} \big[\frac{2\ddot{A}\dot{A}}{A^2} - \frac{2\dot{A}^3}{A^3} \big] + 4 f_T c_0 \frac{\ddot{A}}{A} + 2 f_T (\frac{\dot{A}}{A})^2 c_0 (2m - 1) - (1 + 2m)(f - 2 f_T c_0 (\frac{\dot{A}}{A})^2) = 0. \ (19)$$

This is the modified Raychaudhuri equation, and by setting $m = 1$ in the c_0 parameter, the above equation is reduced to the same equation in isotropic universe, i.e. FRW metric [37] . By the way, it is explicit, that the corresponding Hamiltonian to Lagrangian $\mathcal{L}$ is given by

$$\mathcal{H} = \sum_i \frac{\partial \mathcal{L}}{\partial \dot{q}_i} \dot{q}_i - \mathcal{L}. \qquad (20)$$

Replacing (Eq.14) into (Eq.20), one can rewrite the above Lagrangian density as follows

$$\mathcal{H} = 2 f_T A^{2m-1} c_0 \dot{A}^2 - A^{1+2m}(f - f_T T) + \rho_{m_0}. \qquad (21)$$

Using the zero energy condition, $\mathcal{H} = 0$, [36, 35, 39], we get

$$-2 f_T A^{2m-1} c_0 \dot{A}^2 + A^{1+2m}(f - f_T T) = \rho_{m_0}, \qquad (22)$$

where, it is clear again that by taking $m = 1$ in the c_0 parameter, the above equation end up to one in the modified Friedmann equation, i.e. the $f(T)$ gravity at FRW metric. As a result, we have found that the point-like Lagrangian obtained in (Eq.14) can yield all the correct equations of motion in anisotropic universe, that taken $m = 1$ in the c_0 parameter recovered what is in isotropic universe, i.e. the $f(T)$ gravity equation in FRW metric.

4 Noether Symmetry in f(T) Theory at Anisotropic Universe

As mentioned, one can find the exact solution to the given lagrangian by using Noether symmetry theorem. So in this section, we would like to investigate Noether symmetry in f(T) theory in anisotropic universe. Following references [36, 35, 37] , the generator of Noether symmetry is a killing vector

$$X = \alpha \frac{\partial}{\partial \alpha} + \beta \frac{\partial}{\partial \beta} + \dot{\alpha} \frac{\partial}{\partial \dot{\alpha}} + \dot{\beta} \frac{\partial}{\partial \dot{\beta}}, \qquad (23)$$

where α, β, both are the function of the generalized coordinate of A, T. Requirement of Noether symmetry is that Lie differentiation with respect X to be zero. Hence we get

$$L_X \mathcal{L} = \alpha \frac{\partial \mathcal{L}}{\partial \alpha} + \beta \frac{\partial \mathcal{L}}{\partial \beta} + \dot{\alpha} \frac{\partial \mathcal{L}}{\partial \dot{\alpha}} + \dot{\beta} \frac{\partial \mathcal{L}}{\partial \dot{\beta}} = 0. \tag{24}$$

Therefore, based on Noether symmetry theorem, there should be a motion constant, so-called Noether charge [36, 35].

$$Q_0 = \sum_i \alpha_i \frac{\partial \mathcal{L}}{\partial \dot{\alpha}_i} = \alpha \frac{\partial \mathcal{L}}{\partial \dot{A}} + \beta \frac{\partial \mathcal{L}}{\partial T} = \alpha(4 f_T A^{2m-1} c_0 \dot{A}) = const, \tag{25}$$

where setting $m = 1, c_0 = -3$ in the above equation, recovered the same equation in [37] to isotropic universe. We know that $L_X \mathcal{L} = 0$, meaning $\mathcal{L}$ is constant along the flow generated by X, i.e. (Eq.24[39]. Therefore, evaluating (Eq.24) is a second degree function from $\dot{A}, \dot{T}$, whose coefficients are functions of a and T only. Hence, they have to be zero separately. So, replacing (Eq.13) into (Eq.24) and using the relations $\dot{\alpha} = \partial \alpha / \partial A \dot{A} + \partial \alpha / \partial T \dot{T}$ and $\dot{\beta} = \partial \beta / \partial A \dot{A} + \partial \beta / \partial T \dot{T}$ yield

$$\alpha(1 + 2m)(f - f_T T) + 2\alpha(2m - 1)f_T (\frac{\dot{A}}{A})^2 c_0 - \beta A f_{TT} T + 2\beta f_{TT} \dot{A}^2 A^{-1} c_0 +$$
$$4\frac{\partial \alpha}{\partial A} f_T \dot{A}^2 A^{-1} c_0 + 4\frac{\partial \alpha}{\partial T} \dot{T} f_T \dot{A} A^{-1} c_0 = 0. \tag{26}$$

As mentioned above, the coefficients $\dot{A}^2, \dot{T}\dot{A}$ should be zero, as a result, we get

$$4\frac{\partial \alpha}{\partial T} f_T = 0, \tag{27}$$

$$2(2m - 1)f_T A^{-2}\alpha + 2\beta f_{TT} A^{-1} + 4\frac{\partial \alpha}{\partial A} f_T A^{-1} = 0, \tag{28}$$

$$\alpha(1 + 2m)(f - f_T T) - \beta A f_{TT} T = 0. \tag{29}$$

It is explicit that solutions of (Eqs. 28, 27,29)are given if the explicit form of α, β are obtained, and if at least one of them is different from zero, then Noether symmetry exist[35]. From (Eq.27), it is clear that α is independent of T, so it is merely a function of A. In addition, from (Eq.29), we get

$$\alpha(1 + 2m)(f - f_T T) = \beta A f_{TT} T. \tag{30}$$

By substituting (Eq.30) in to (Eq.28), we get

$$2(2m - 1)f_T T A^{-2}\alpha + 2\alpha(1 + 2m)(f - f_T T)A^{-2} + 4f_T A^{-1} T \frac{\partial \alpha}{\partial A} = 0. \tag{31}$$

By separation of variables, one can transform the above equation to two independent differential equations as follow

$$1 - \frac{A}{\alpha} \frac{\partial \alpha}{\partial A} = \frac{(1 + 2m)f}{2f_T T}. \tag{32}$$

Since Right and left hand side are independent, hence, they must be equal to a same constant, that fore convenience, we set $\frac{1+2m}{n}$. As a result, (Eq.32) is separated into two ordinary

differential equations as

$$1 - \frac{A}{\alpha}\frac{\partial\alpha}{\partial A} = \frac{1+2m}{2n}, \tag{33}$$

$$\frac{(1+2m)f}{2f_T T} = \frac{1+2m}{2n}. \tag{34}$$

It is readily obtained the solutions of these two above equation as follow

$$f = \mu T^n, \tag{35}$$

$$\alpha = \alpha_0 A^{\frac{2n-1-2m}{2n}}, \tag{36}$$

where, again the above equation is reduced into the same equation in isotropic universe by setting $m = 1$, i.e. [37]; hence it is the desired one and μ, α_0 are integral constants. Substituting (Eqs.35, 36) into (Eq.30) we get

$$\beta = -\frac{\alpha_0\mu(1+2m)}{n}A^{-\frac{1+2m}{2n}}T. \tag{37}$$

Up till now, we obtained the non-zero solution of $f(T), \alpha, \beta$. Therefore, Noether symmetry exists in anisotropic universe on Bianchi type I. Now, we try to obtain a solution of scale factor for this $f(T)$ function. Hence substituting, the (Eqs.35,36,37) into (Eq.25) yields

$$\dot{A}A^{c_2} = (\frac{c_1}{c_0})^{\frac{1}{2}}, \tag{38}$$

where, $c_1 = (Q_0/4\mu nc_0\alpha)^{1/n-1}, c_2 = \frac{4m^2+2m-4mn-1}{4m(n-1)}$. It is readily obtained the solution of (38) as follow

$$A = (1+c_2)^{\frac{1}{1+c_2}}\left[(\frac{c_1}{c_0})^{\frac{1}{2}}t - c_3\right]^{\frac{1}{1+c_2}}, \tag{39}$$

where c_3 is integral constant. From requirement $a(t = 0) = 0$, it is easy to see that the constant c_3 is zero. As a result, $A \sim t^{\frac{1}{1+c_2}}$. Therefore, as mentioned, relation between scale factor a and component metric A in anisotropic Bianchi type I with assuming, $B = C = A^m$ is $a^3 = (ABC) = A^{1+2m}$, hence

$$a \sim t^{\frac{1+2m}{3(1+c_2)}}. \tag{40}$$

Note that, requirement of positive expansion, $\ddot{a} > 0$ requiring a constrained between the n and m, parameter as following

$$n - 1 < \frac{3m}{4+2m}. \tag{41}$$

It is clear, that one can readily obtained physical quantity corresponding to the exact solution a and $f(T)$ namely, $H, \dot{H}, \sigma^2$, and equation of state ω, that in this work, it is not our scope.

5   Discussion

As it is well known, symmetry plays a crucial role in the theoretical physics. On other hand, the Noether symmetry is a useful procedure to select models motivated at a fundamental

level, and discover the exact solution to the given lagrangian. In this work, Noether symmetry in f(T) theory on A spatially homogeneous and anisotropic Bianchi type I universe have considered. We have addressed the Lagrangian formalism of f(T) theory in anisotropic universe, and a Lagrangian form was obtained. The point-like Lagrangian was clearly constructed. The explicit form of f(T) theory and the corresponding exact solution were found by requirement of Noether symmetry and Noether charge. A power-law f(T), have obtained in the anisotropic universe with power- law scale factor, that can satisfy the requirement of the Noether symmetry. It was regarded that positive expansion is satisfied. Our main conclusions can be summarized as follows

- A exact solution have been obtained to $f(T), a(t)$, that is reduced to those value in FRW metric with selecting the m parameter, equal one, i.e. $m = 1$ and $c_0 = -3$

- Requirement of positive acceleration have obtained a constrained between m and n parameter, i.e. $n - 1 < \frac{3m}{4+2m}$

- To regain the equation lagrangian form in the FRW metric, it was required $c_0 \neq 0, -2/7$.

- It was obtained a energy density matter form by the zero energy condition, $\mathcal{H} = 0$,

- We have obtained exact solution of scale factor a by Noether charge condition.

- At last,we have seen that the resulting f(T) theory from Noether symmetry can be study in anisotropic universe that may be, plays an important role at early universe.

References

[1] Brans. C., Dicke. R. H.,1996, Phys. Rev 124, 925–935

[2] Justin. Khoury., Amanda. Weltman., 2004, Annalen der Physik 69, 044026 .

[3] David F. Mota., John D. Barrow., 2004, Physics Letters B 581, 141–146 .

[4] Saaidi. Kh., Mohammadi. A., Sheikhahmadi. H., 2011, Phys. Rev. D 83, 104019.

[5] David. Wands., 1994, Classical and Quantum Gravity 11 269

[6] Nojiri. Shin'ichi., Odintsov. Sergei D.,2006, Phys. Rev. D 74, 086005 .

[7] Guarnizo. Alejandro., Castaeda. Leonardo., et al., 2010, General Relativity and Gravitation 42, 2713-2728.

[8] Saaidi. KH., Aghamohammadi. A., et al., 2012, International Journal of Modern Physics D 21, 1250057.

[9] Chao-Qiang Geng., Chung-Chi Lee., et al.,2011, Physics Letters B 704, 384 - 387.

[10] Linder. Eric V.,2010, Phys. Rev. D 81 127301.

[11] Bamba. Kazuharu., Geng. Chao-Qiang., et al.,2011, Journal of Cosmology and Astroparticle Physics 2011, 021.

[12] Aghamohammadi. A., 2014, Astrophysics and Space Science 352, 1–5 .

[13] Bengochea, Gabriel R.,2009, Ferraro, Rafael., Phys. Rev. D 79, 124019 5.

[14] Ferraro. Rafael., Fiorini. Franco.,2007, Phys. Rev. D 75, 084031.

[15] Saridakis.E.N.,2008, Phys. Lett. B 660, 138.

[16] Zhang.J., Zhang. X., et al., 2007, Eur. Phys. J. C 52, 693.

[17] Cai. R.G.,2007, Phys. Lett. B 657, 228.

[18] Wei. H., Cai.R.G., 2009, Eur. Phys. J. C 59, 99.

[19] Wei.H., Cai. R.G.,2008, Phys. Lett. B 660, 113.

[20] Wei. H., Cai.R.G.,2008, Phys. Lett. B 663, 1.

[21] Wu. J.-P., Ma. D.-Z., et al., 2008, Phys. Lett. B 663, 152.

[22] Neupane. I.P., 2009, Phys. Lett. B 673, 111.

[23] Zhang. J.,Zhang. X.,Liu. H., 2008, Eur. Phys. J. C 54, 303.

[24] Li.Y.H., Ma. J.Z., Cui.J.L.,et al, 2011, Sci. China Phys. Mech. Astron. 54, 1367.

[25] E. Komatsu., *et al.*, 2009, Astrophys. J. Suppl. Ser. 180, 330.

[26] Bertschinger. E., 1994, Physica D 77, 354.

[27] Brevik. I., Pettersen.S.V., 1997, Phys. Rev. D 56, 3322.

[28] Khalatnikov.I.M., kamenshchik. A.Yu., 2003, Phys. Lett. B **553**, 119.

[29] Rodrigues, D.C.,2008, Phys. Rev. D 77, 023534.

[30] Koivisto, T., Mota, D.F.,2008b, Astrophys. J 679, 1.

[31] Yadav, A.K., Saha, B.,2012, Astrophys. Space Sci 337, 759

[32] Sharif, M., Rani, S., 2011, Mod. Phys. Lett. A 26, 1657.

[33] Ferraro, R., Fiorini, F.,2007, Phys. Rev. D 75, 084031. arXiv:gr-qc/ 0610067.

[34] Bengochea, G.R., Ferraro, R., 2009, Phys. Rev. D 79, 124019. arXiv: 0812.1205

[35] Vakili.B.,2008, Phys. Lett. B 664, 16 [arXiv:0804.3449].

[36] Capozziello.S., De Felice. A., 2008 JCAP 0808, 016 [arXiv:0804.2163]; Capozziello.S., Lambiase,G.,2000, Gen. Rel. Grav. 32, 673 [gr-qc/9912083].

[37] Wei. H., Guo. X.J., Wang, L.F., 2012, Phys. Lett. B , 707, 298304.

[38] Fayaz. V., Hossienkhani. H., et al., 2014, Astrophys. Space Sci. 353, 301.

[39] de Ritis.R., et al., 1990, Phys. Rev. D 42, 1091.

Effect of random telegraph noise on entanglement and nonlocality of a qubit-qutrit system

Hakimeh Jaghouri[1] · Samira Nazifkar[2]

[1] Quchan University of Advanced Technology, Quchan, Iran

[2] Department of Physics, University of Neyshabur, Neyshabur, Iran

Abstract. We study the evolution of entanglement and nonlocality of a non-interacting qubit-qutrit system under the effect of random telegraph noise (RTN) in independent and common environments in Markovian and non-Markovian regimes. We investigate the dynamics of qubit-qutrit system for different initial states. These systems could be existed in far astronomical objects. A monotone decay of the nonlocality (entanglement) is found in the Markov regime, while for non-Markovian noise, phenomena of sudden change (death) and revival occurs. We find that the preserving nonlocality (entanglement) depends on initial state of the system in common and independent environments; so, we can not strictly conclude that independent or common environments are more robust against the noise.

1   Introduction

A distinctive property of the quantum world is nonlocality which differs it from the classical world. Nonlocality could be used in quantum information processing tasks to improve the efficiency. It prepares a new classification for bipartite states, which might be useful in quantum state steering [1]. In quantum mechanics the nonlocality shows itself in two different scenarios, the Aharonov-Bohm effect and the entanglement (the Einstein-Podolsky-Rosen correlations). Nonlocality in quantum usually refers to correlations which local hidden variable theory can not describe them while nonlocality has been shown by Bells inequalities widely [2]. Different measures have been proposed for detecting the nonclassical correlations which can not be found by entanglement measures [3, 4, 5, 6]. On the other hand, there are unavoidable interactions between system and its surround environment which induces decoherence. Decoherence is the main factor which destroys quantum properties as correlations, so investigation of evolution of quantum correlations on these systems sounds interesting for making quantum device with high performance. The combination of general relativity and quantum field theory predicts that black hole emits Hawking radiation [7, 8]. In some numerical simulations, spontaneous Hawking radiation emanates from an analogue black hole in an atomic Bose-Einstein condensate which is stimulated by quantum vacuum fluctuations[7, 8]. They observe some correlations and entanglement between the Hawking particles outside the black hole and the partner particles inside. They find that the pairs with high energy are entangled, while the pairs with low energy are not entangled so in this paper we consider both states (entangled and separable states) [8]. The study of the thermodynamics of interaction of black holes with entangled particles is very interesting [8, 9, 10, 11, 12, 13].

2   The model

Particles with spin-$\frac{1}{2}$ (two-level systems) and spin-1 (three-level systems) are called qubit and qutrit respectively. Karpat and Gedik have been studied the evolution of quantum correlations and entanglement for a qubit-qutrit system in common and independent environments under the effect of classical dephasing noise in the Markovian regime [14]. So, it seems interesting to study the dynamics of nonlocality and the entanglement of a qubit-qutrit system under other classical noise sources as RTN. We consider a model of a qubit-qutrit system which has been prepared in different initial states as entangled (ρ_E), separated (ρ_S) and Bell-like (ρ_B) states. The system is under a random telegraph noise (RTN) of common and independent environments in Markovian and non-Markovian regimes.

The Hamiltonian of the dynamics of the qubit-qutrit system under RTN is defined as [15]

$$H(t) = H^A(t) \otimes \mathbb{I}^B + \mathbb{I}^A \otimes H^B(t), \tag{1}$$

where $\mathbb{I}^A$ ($\mathbb{I}^B$) is the identity operator in the subspace of qutbit (qutrit) and H^A (H^B) is the single qubit (qutrit) Hamiltonian which is defined as

$$H^A(t) = \omega_0^A \mathbb{I}^A + \nu \zeta^A(t) s_z{}^A \tag{2}$$
$$H^B(t) = \omega_0^B \mathbb{I}^B + \nu \zeta^B(t) S_z{}^B.$$

Where $\hbar = 1$, so ω_0^A (ω_0^B) is the energy of system A (B) in absence of noise, s_z^A (S_z^B) is spin-$\frac{1}{2}$ (spin-1) operator in z direction and the system-environment coupling constant is ν. The Hamiltonian given in Eq. (1) is stochastic because of randomness of the parameter $\zeta^{A(B)}(t)$. This parameter describes a fluctuator which flips between the values ± 1 randomly with rate γ so the quantum states evolves stochastically.

Random phase factor is $\varphi^{A(B)}(t) = -\nu \int_0^t ds\, \zeta^{A(B)}(s)$. One can get the qubit-qutrit density matrix by the average over the random phase factor as $\rho(t) = \left\langle \left\langle \rho(\varphi^A(t), \varphi^B(t)) \right\rangle_{\varphi^A} \right\rangle_{\varphi^B}$ [15].

The autocorrelation function is $\left\langle \delta\zeta^{A(B)}(t)\delta\zeta^{A(B)}(0) \right\rangle = e^{-2\gamma t}$. The ratio of the system-environment coupling (ν) and the switching rate (γ) shows the non-Markovian and Markovian behaviors of system. For $\nu \gg \gamma$ (or $\alpha = \frac{\nu}{\gamma} \gg 1$), the system is in non-Markovian regime, while for $\nu \ll \gamma$ (or $\alpha = \frac{\nu}{\gamma} \ll 1$), it is in Markovian regime. The noise parameters of the qubit and qutrit ($\zeta^A(t)$ and $\zeta^B(t)$) are different for independent environments ($\zeta^A(t) \neq \zeta^B(t)$) while they are same for common environment ($\zeta^A(t) = \zeta^B(t) = \zeta(t)$). The average phase factor expresses as

$$\Delta_{n\nu}(t) = \begin{array}{ll} e^{-\gamma t} & \left[cosh(\delta_{n\nu}t) + \dfrac{\gamma}{\delta_{n\nu}} sinh(\delta_{n\nu}t) \right] \quad \gamma > n\nu \\[3mm] e^{-\gamma t} & \left[cos(\delta_{n\nu}t) + \dfrac{\gamma}{\delta_{n\nu}} sin(\delta_{n\nu}t) \right] \qquad \gamma < n\nu, \end{array} \tag{3}$$

where $\delta_{n\nu} = \sqrt{|(n\nu)^2 - \gamma^2|}$ and $n \in \mathbb{N}$.

The initial state of qubit-qutrit system could be defined as Bell-like state (ρ_B), entangled state (ρ_E) and separable state (ρ_S).

$$\rho_B(x) = |\psi\rangle\langle\psi|, \qquad |\psi\rangle = \sqrt{x}\,|11\rangle + \sqrt{1-x}\,|33\rangle, \tag{4}$$

$$\begin{aligned} \rho_E(0) = {} & \frac{p}{2}(|11\rangle\langle11| + |12\rangle\langle12| + |11\rangle\langle23| + |22\rangle\langle22| + |23\rangle\langle23| + |23\rangle\langle11|) \\ & + \frac{1-2p}{2}(|13\rangle\langle13| + |13\rangle\langle21| + |21\rangle\langle13| + |21\rangle\langle21|) \end{aligned} \tag{5}$$

and

$$\rho_S(0) \;=\; \frac{r}{2}(|11\rangle\langle 11| + |12\rangle\langle 12| + |11\rangle\langle 23| + |22\rangle\langle 22| + |23\rangle\langle 23| + |23\rangle\langle 11| \tag{6}$$
$$+\;\; |13\rangle\langle 21| + |21\rangle\langle 13|) + \frac{1-2r}{2}(|13\rangle\langle 13| + |21\rangle\langle 21|)$$

where $0 \le x \le 1$, $0 \le p \le \frac{1}{2}$ and $0 \le r \le \frac{1}{3}$. For $p = \frac{1}{3}$, the state ρ_E is separable.
The qubit-qutrit system is under RTN, its density matrices evolution for Bell-like initial state and common and independent environments are

$$\rho_B^{ie(ce)}(t) = \begin{bmatrix} x & 0 & 0 & 0 & 0 & \sqrt{x\,(1-x)}F^{ie(ce)} \\ 0 & 0 & 0 & 0 & 0 & 0 \\ 0 & 0 & 0 & 0 & 0 & 0 \\ 0 & 0 & 0 & 0 & 0 & 0 \\ 0 & 0 & 0 & 0 & 0 & 0 \\ \sqrt{x\,(1-x)}F^{ie(ce)} & 0 & 0 & 0 & 0 & 1-x \end{bmatrix}. \tag{7}$$

Qubit-qutrit system evolution for entangled initial state in independent and common environments are

$$\rho_E^{ie}(t) = \frac{1}{2}\begin{bmatrix} p & 0 & 0 & 0 & 0 & pF^{ie} \\ 0 & p & 0 & 0 & 0 & 0 \\ 0 & 0 & 1-2p & (1-2p)\,F^{ie} & 0 & 0 \\ 0 & 0 & (1-2p)\,F^{ie} & 1-2p & 0 & 0 \\ 0 & 0 & 0 & 0 & p & 0 \\ pF^{ie} & 0 & 0 & 0 & 0 & p \end{bmatrix}, \tag{8}$$

$$\rho_E^{ce}(t) = \frac{1}{2}\begin{bmatrix} p & 0 & 0 & 0 & 0 & pF^{ce} \\ 0 & p & 0 & 0 & 0 & 0 \\ 0 & 0 & 1-2p & 1-2p & 0 & 0 \\ 0 & 0 & 1-2p & 1-2p & 0 & 0 \\ 0 & 0 & 0 & 0 & p & 0 \\ pF^{ce} & 0 & 0 & 0 & 0 & p \end{bmatrix}.$$

Evolution of the system for an initial separable state will be

$$\rho_S^{ie}(t) = \frac{1}{2}\begin{bmatrix} r & 0 & 0 & 0 & 0 & rF^{ie} \\ 0 & r & 0 & 0 & 0 & 0 \\ 0 & 0 & 1-2r & rF^{ie} & 0 & 0 \\ 0 & 0 & rF^{ie} & 1-2r & 0 & 0 \\ 0 & 0 & 0 & 0 & r & 0 \\ rF^{ie} & 0 & 0 & 0 & 0 & r \end{bmatrix}, \tag{9}$$

$$\rho_S^{ce}(t) \;=\; \frac{1}{2} \begin{bmatrix} r & 0 & 0 & 0 & 0 & rF^{ce} \\ 0 & r & 0 & 0 & 0 & 0 \\ 0 & 0 & 1-2r & r & 0 & 0 \\ 0 & 0 & r & 1-2r & 0 & 0 \\ 0 & 0 & 0 & 0 & r & 0 \\ rF^{ce} & 0 & 0 & 0 & 0 & r \end{bmatrix}$$

with $F^{ie} = \Delta_{2\nu}^2(t)$, $F^{ce} = \Delta_{4\nu}(t)$ and $n = 2$ ($n = 4$) for independent (common) environments.

Evolution of entanglement

At first, we apply negativity as an estimator to quantify entanglement of the system which is defined as

$$E(\rho^{AB}) = \frac{\sum_i(|\eta_i| - \eta_i)}{2}, \tag{10}$$

where η_is are the eigenvalues of the partial transpose of ρ^{AB} with respect to the subsystem "A" [16].

The negativity has been obtained for different initial conditions of the system in independent (common) environments. For initial Bell-like state, the negativity has been obtained as

$$E_B^{ce(ie)} = 2|F^{ce(ie)}|\sqrt{-x^2 + x} \tag{11}$$

and for initial entangled state in independent (common) environments, the negativity is

$$
\begin{aligned}
E_E^{ce} &= \frac{1}{2}(p(F^{ce} - 1) + |3p - 1| + |2p + pF^{ce} - 1|), \\
E_E^{ie} &= \frac{1}{2}(p((F^{ce})^2 - 1) + |2p - 1 + p(F^{ce})^2| + |p - (F^{ce})^2 + 2p(F^{ce})^2| \\
&\quad + |2p(F^{ce})^2 - p - (F^{ce})^2|).
\end{aligned} \tag{12}
$$

For an initial Bell-like state ($x = \frac{1}{2}$), Fig. 1.a shows negativity for independent and common environments for Markovian regime. It demonstrates when environments are independent and the entanglement of the system is more robust. One can say when the qubit-qutrit is coupled with a common environment, there is a kind of interaction mediator between qubit subsystem and qutrit subsystem. For non-Markovian regime, phenomena of sudden death and revival are demonstrated in Fig1.b. One can see that in the common environment, entanglement is more robust in comparison with case of the independent environments.

As Figs. 1.c and 1.d show for the case $p = \frac{1}{4}$, entanglement in common environment is constant while in independent environments for Markovian regime has sudden death and for non-Markovian regime has sudden death and revival entanglement. This behavior of system seems a remarkable result of our work, because in before studies have been emphasized that robustness of entanglement happens for independent environments in Markovian regime and it also happens for common environment in non-Markovian regime. We investigate entanglement of the system, for initial entangled state with $p = 0.45$. The evolution of entanglement has been shown in Fig.1.c and 1.d for Markovian and non-Markovian regime respectively. One can see that these figures verify previous studies.
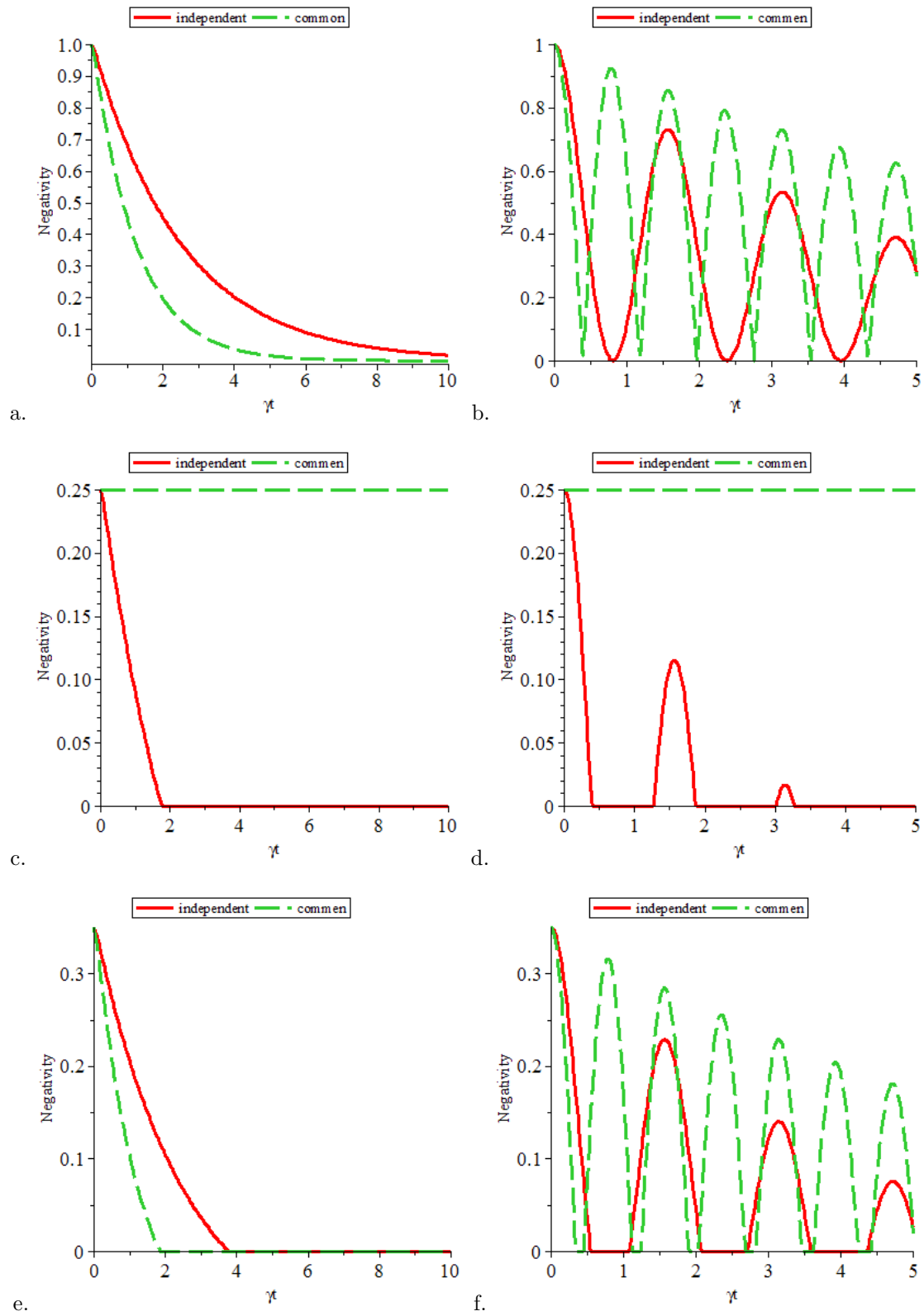
Figure 1: Comparision of negativity for common and independent environments. a,b: $x = \frac{1}{2}$, c,d:$p = \frac{1}{4}$ and e,f:$p = 0.45$. a,c,e $\alpha = 0.1$ and b,d,f $\alpha = 10$.

Evolution of nonlocality

The nonlocality of a physical system shows quantumness which could be measured by measurement induced nonlocality (MIN). This measure is defined as

$$N(\rho^{AB}) = \max_{\Pi^A} ||\rho^{AB} - \Pi^A(\rho^{AB})||^2, \tag{13}$$

the $\{\Pi^A\}$ is projective measurements set which has been made of eigenstates of ρ^A. For any operator, Hilbert-Schmidt norm is defined as $||K|| = \sqrt{tr(K^\dagger K)}$. The spaces that have all linear operators on H^A and H^B respectively are $L(H^A)$ and $L(H^B)$. The $L(H^A)$ and $L(H^B)$ have orthonormal bases as $X_i(i = 1, 2, ..., m^2)$ and $Y_j(j = 1, 2, ..., n^2)$ respectively. A bipartite state in $H^A \otimes H^B$ can be written as

$$\rho = \frac{1}{mn}\mathbb{I}^A \otimes \mathbb{I}^B + \sum_{i=2}^{m^2} x_i X_i \otimes \frac{\mathbb{I}^B}{\sqrt{n}} + \sum_{j=2}^{n^2} \frac{\mathbb{I}^A}{\sqrt{m}} \otimes y_j Y_j + \sum_{i=2}^{m^2}\sum_{j=2}^{n^2} t_{ij} X_i \otimes Y_j. \tag{14}$$

Where $X_1 = \frac{\mathbb{I}}{\sqrt{m}}$, $Y_1 = \frac{\mathbb{I}}{\sqrt{n}}$, $\{X_i, i = 2, ..., m^2\}$ and $\{Y_j, j = 2, ..., n^2\}$ are defined as generators of $SU(m)$ and $SU(n)$, respectively. Coefficients in Eq. (14) are

$$x_i = \frac{m}{2}Tr(\rho X_i \otimes \mathbb{I}_n), y_j = \frac{n}{2}Tr(\rho\mathbb{I}_m \otimes X_j) \text{ and } t_{ij} = \frac{mn}{4}Tr(\rho X_i \otimes Y_j) \tag{15}$$

$\vec{x} = [x_i]$, $\vec{y} = [y_j]$ and $T = [t_{ij}]$. For a $2 \otimes n$ dimensional system from Eq. (14) MIN, has following form

$$N(\rho^{AB}) = Tr(TT^t) - \lambda_{min} \tag{16}$$

Where TT^t is a 3×3 dimensional matrix, and λ_{min} is its minimum eigenvalue.
For initial Bell-like state in common and independent environments, we calculate nonlocality as

$$\begin{aligned}
N_B^{ce(ie)} &= 8\,x(F^{ce(ie)})^2 - 8\,x^2(F^{ce(ie)})^2 \\
&+ \frac{4}{3}(x^2 - x + 1 - \min\left(3\,x(F^{ce(ie)})^2 - 3\,x^2(F^{ce(ie)})^2, x^2 - x + 1\right)).
\end{aligned} \tag{17}$$

The evolution of MIN for an initial entangled state in common and independent environments is

$$\begin{aligned}
N_E^{ce} &= 2\,p^2(F^{ce})^2 + 3 - 14\,p + 17\,p^2 - \min(9\,p^2 - 6\,p + 1, p^2(F^{ce})^2 - 2\,pF^{ce} + 4, \\
&\quad p^2 F^{ce} + 1 - 4\,p + 4\,p^2, p^2(F^{ce})^2 + 2\,pF^{ce} - 4\,p^2 F^{ce} + 1 - 4\,p + 4\,p^2) \\
N_E^{ie} &= 10\,p^2(F^{ie})^2 - 8\,(F^{ie})^2 p + 2\,(F^{ie})^2 + 9\,p^2 - 6\,p + 1 \\
&- \min\left(9\,p^2 - 6\,p + 1, p^2(F^{ie})^2 - 2\,(F^{ie})^2 p + (F^{ie})^2, 9\,p^2(F^{ie})^2 - 6\,(F^{ie})^2 p + (F^{ie})^2\right).
\end{aligned} \tag{18}$$

For an initial state with zero entanglement (separable) in common and independent environments, MIN will be

$$\begin{aligned}
N_S^{ce} &= 2\,r^2(F^{ce})^2 + 11\,r^2 - 6\,r + 1 \\
&- \min\left[9\,r^2 - 6\,r + 1, r^2(F^{ce})^2 - 2\,r^2 F^{ce} + r^2, r^2(F^{ce})^2 + 2\,r^2 F^{ce} + r^2\right] \\
N_S^{ie} &= 4\,r^2(F^{ie})^2 + 9\,r^2 - 6\,r + 1 - \min\left[0, 4\,r^2(F^{ie})^2, 9\,r^2 - 6\,r + 1\right].
\end{aligned} \tag{19}$$

One can find from Fig 2.a, evolution of nonlocality for initial Bell-like state with $x = \frac{1}{2}$ in Markovian regime which shows that nonlocality in independent environments are more

robust than common type. With the passage of time nonlocality goes to a fixed value in both types of environments. For non-Markovian case, Fig. 2.b shows that in common and independent environments, MIN has sudden change and revival. In the case of common environment, MIN is more robust than independent environments against the noise. These behaviors of MIN are the same with entanglement behaviors which have been studied in previous section.

We demonstrate in Fig 2.c that nonlocality decreases monotonically and at the final stage, it goes to a fixed value in Markovian regime. In non-Markovian regime, MIN has a sudden change and revival behavior. In the common environment, nonlocality of the system is more robust than independent environments in two regimes (Markovian and non-Markovian). We remind that for a separable initial state, entanglement is zero while there is nonlocality.

Result

We have shown the evolution of entanglement and nonlocality for different initial states and different conditions. Our finding shows that for a separable state, there is nonlocality but entanglement is zero. Robustness of entanglement and nonlocality, in common or independent environment, depend on initial state for Markovian regime. This result is different from results of previous studies. While for non-Markovian case in common environment, entanglement and MIN are more robust than independent environments which are interesting results of our work.

References

[1] N. Brunner, Nature physics **6**, 842 (2010).

[2] J. S. Bell, Physics (N.Y.)1, 195 (1964).

[3] S. Luo, Phys. Rev. A **77** 022301 (2008).

[4] H. Ollivier, W.H. Zurek, Phys. Rev. Lett. **88** 017901 (2001).

[5] S. Luo and S. Fu, Phys. Rev. Lett **106**, 120401 (2011).

[6] H. Jaghouri, M. Sarbishaei and K. Javidan, Quantum Information Processing **16** (2017).

[7] J. Steinhauer, Nature Physics, **10**, 864 (2014).

[8] J. Steinhauer, arXiv:1510.00621 (2015).

[9] P. Levay, M. Saniga, P. Vrana, P. Pracna, Phys. Rev. D, **79**, 084036 (2009).

[10] D. Ahn , M. S. Kim, Phys. Rev. D **78** 064025 (2008).

[11] J. Gomez, Proceedings of science, 015 (2009).

[12] D. Ahn, JHEP 0703, 021 (2007).

[13] H. Jaghouri, M. Sarbishaei and K. Javidan, Iranian Journal of Astronomy and Astrophysics **2**, 2 (2015).

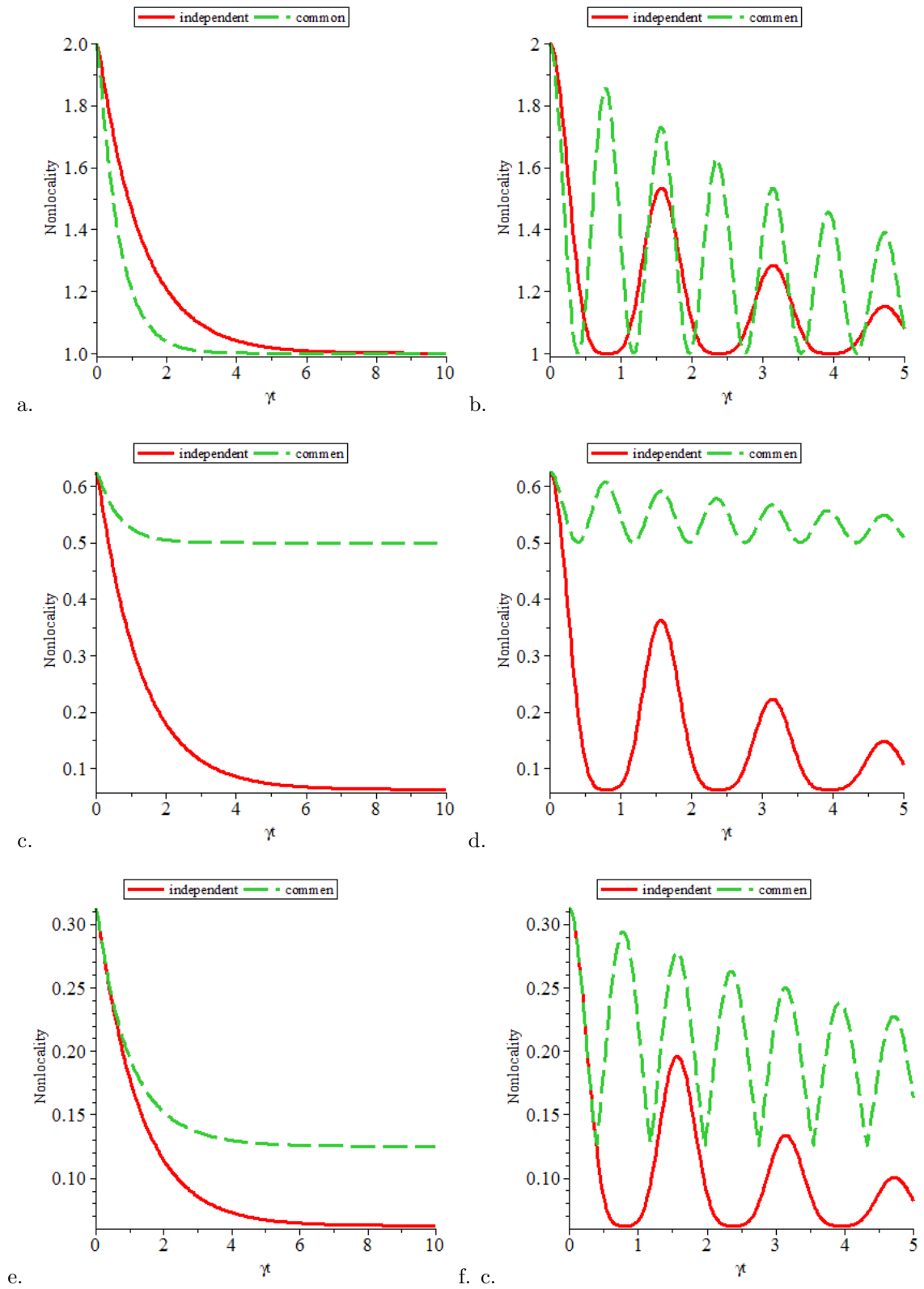[14] G. Karpat, Z. Gedik, Phys. Lett. A **375**, 4166 (2011).

Figure 2: Comparision of nonlocality for common and independent environments. a,b: $x = \frac{1}{2}$, c,d:$r = \frac{1}{4}$ and e,f:$s = \frac{1}{4}$. a,c,e: $\alpha = 0.1$ and b,d,f: $\alpha = 10$.

[15] A. T. Tsokeng, M. Tchoffo and L. C. Fai. Quantum Information Processing, **16**, 191 (2017).

[16] A. Peres, Phys. Rev. Lett. **77**, 1413 (1996).

Pulsating red giant and supergiant stars in the Local Group dwarf galaxy Andromeda I

Elham Saremi[1] · Abbas Abedi[1] · Atefeh Javadi[2] · Jacco van Loon[3] · Habib Khosroshahi[2]

[1] Department of Physics, Faculty of Science, University of Birjand, Birjand, P.O.Box 97175-615, Iran; email: saremi@birjand.ac.ir
[2] School of Astronomy, Institute for Research in Fundamental Sciences (IPM), Tehran, P.O.Box 19395-5531, Iran;
[3] Lennard-Jones Laboratories, Keele University, ST5 5BG, UK

Abstract. We have conducted an optical long-term monitoring survey of the majority of dwarf galaxies in the Local Group, with the Isaac Newton Telescope (INT), to identify the long period variable (LPV) stars. LPV stars vary on timescales of months to years, and reach the largest amplitudes of their brightness variations at optical wavelengths, due to the changing temperature. They trace stellar populations as young as ~ 30 Myr to as old as ~ 10 Gyr whose identification is one of the best ways to reconstruct the star formation history.

The system of galactic satellites of the large Andromeda spiral galaxy (M 31) forms one of the key targets of our monitoring survey. In this first paper in the series, we present the first results from the survey in the form of a census of LPV stars in Andromeda I (And I) dwarf galaxy.

Photometry was obtained for 10585 stars in a 0.07 square degree field, of which 116 stars were found to be variable, most of which are Asymptotic Giant Branch (AGB) stars. Our data were matched to mid-infrared photometry from the *Spitzer* Space Telescope, and to optical catalogues of variable stars from the *Hubble* Space Telescope.

Keywords: stars: evolution, stars: red giants, supergiants, stars: mass-loss, stars: oscillations, galaxies: individual: Andromeda I, galaxies: stellar content

1 Introduction

Dwarf galaxies are the most common type of galaxies in the Universe, and the building blocks of more massive galaxies in hierarchical formation scenarios. The great variety in terms of stellar mass, luminosity, gas content, metallicity and surface brightness reflect the complex dynamical and astrophysical processes that drive galaxy evolution. Also, they represent the smallest scales on which astronomers are able to detect dark matter [1, 2, 3, 4, 5]. Therefore, their study is crucial for improving the cosmological models and our understanding of galaxy evolution. Naturally, our home, the Local Group (LG), is the best place to study dwarfs since their individual stars can be resolved and evolutionary histories can be derived in great detail.

The LG comprises dwarf galaxies of all diversity: dwarf spheroidals (dSphs), dwarf irregulars (dIrrs), and transition (dTrans) galaxies. DSphs are found in denser environments and have lower luminosities than dIrrs. They show no evidence of recent star formation (within the last 200 Myr). DTrans are located in similar environments occupied by dIrr galaxies; however, their luminosity and the star formation history are more comparable to dSphs [6, 7, 8, 9, 10, 11].

We have conducted an optical monitoring survey of the majority of dwarf galaxies in the LG, with the Isaac Newton Telescope (INT) for a duration of three years [12]. Our main objective is to identify all Long Period Variable stars (LPVs) in them. Then, we can determine the star formation histories from the mass function of LPVs, with a method that we successfully applied in some of the LG galaxies [13, 14, 15, 16, 17]. The most evolved stars with low to intermediate birth mass, $0.8 - 8\ M_\odot$, at the tip of the Asymptotic Giant Branch (AGB), and somewhat more massive red supergiants (RSGs), show brightness variations on timescales of ≈ 100 to > 1000 days due to radial pulsations and this makes them powerful tools to trace stellar populations as young as ~ 30 Myr to as old as the oldest Globular Clusters.

In this paper, we present a first census of LPV stars in Andromeda I (And I) dwarf galaxy with data from our survey. And I is a bright dSph ($M_\mathrm{V} = -11.8 \pm 0.1$) mag [18], that was initially discovered on photographic plates by van den Bergh (1972). It lies some $3.3°$ from the center of M 31 at a position angle of $\sim 135°$ relative to the M 31 major axis [19]. Considerable efforts have been made to study the structure and properties of And I. For instance, McConnachie & Irwin (2006) have shown that And I is a strongly disrupted satellite of M 31. Also, they have derived some of the structural parameters such as position angle (22 ± 15 deg), ellipticity (0.22 ± 0.04), tidal radius (10.4 ± 0.9 arcmin) and half-light radius (2.8 arcmin) for this galaxy [18]. Kalirai et al. (2010) with spectroscopic data of And I have calculated the mean radial velocity 375.8 ± 1.4 km/s and intrinsic dispersion velocity 10.6 ± 1.1 km/s. They determined a metallicity of -1.45 ± 0.04 using theoretical isochrones [20]. Recent studies have shown that a large fraction of the M 31 dwarf galaxies such as And I have extended star formation histories, and appear inconsistent with an early truncation of their star formation histories [21].

The distance to And I has been determined *via* several methods. Da Costa et al. (1996) determined a distance of 810 ± 30 kpc by using Horizontal Branch stars, i.e. a distance modulus 24.55 ± 0.08 mag [19]. By using the tip of the red giant branch (RGB), McConnachie et al. (2004) found a distance of 735 ± 23 kpc, i.e. a distance modulus 24.33 ± 0.07 mag [22]. However, Conn et al. (2012) revised this to $\mu = 24.31 \pm 0.05$ mag. Martínez-Vázquez et al. (2017) calculated the distance based on the properties of the RR Lyrae stars and several independent techniques [23]: the reddening-free period-Wesenheit relations (24.49 ± 0.08), the luminosity-metallicity (M_V versus [Fe/H]) relation (24.54 ± 0.16), the first overtone blue edge relation (24.49 ± 0.10) and the RGB tip method (24.49 ± 0.12) [24]. In this paper, we adopted the last one, i.e. a distance modulus 24.49 ± 0.12 mag.

This paper is organized as follows: In Section 2, we describe the observations performed for this data set. Section 3 explains the data reduction and photometry method. The quality of data is discussed in section 4 and our method to detect LPVs is presented in Section 5. The discussion follows in Section 6.

2   Description of observations

Over the period June 2015 – October 2017, we used the Wide Field Camera (WFC) to conduct a survey of the majority of dwarf galaxies in the LG. The WFC is an optical mosaic camera at the 2.5m Isaac Newton Telescope (INT) of the Observatorio del Roque de los Muchachos (La Palma). It consists of four 2048×4096 CCDs, with a pixel size of 0.33 arcsec/pixel. The edge to edge limit of the mosaic, neglecting the $\sim 1'$ inter-chip spacing, is $34.2'$.

LPVs vary on timescales from ~ 100 days for low-mass AGB stars to ~ 1300 days for the dustiest massive AGB stars. Although we are not aiming to determine accurate periods,

Table 1: Log of WFC observations of And I dwarf galaxy.

Date (y m d)	Julian date	Epoch	Filter	$t_{\exp}$ (sec)	Airmass
2016 02 09	2457428.3494	2	i	60	1.475
2016 06 14	2457553.6758	3	i	60	1.612
2016 08 10	2457610.6268	4	i	60	1.086
2016 08 12	2457612.6985	4	V	80	1.014
2016 10 20	2457681.6113	5	i	60	1.189
2016 10 20	2457681.6286	5	V	80	1.263
2017 01 29	2457783.4433	6	i	60	2.393
2017 08 01	2457966.7014	7	i	60	1.018
2017 08 01	2457966.7174	7	V	80	1.014
2017 09 01	2457997.5625	8	i	60	1.087
2017 09 01	2457997.5799	8	V	80	1.054
2017 10 06	2458033.4097	9	i	60	1.286
2017 10 08	2458034.5389	9	V	80	1.014

to identify the LPVs and to determine their amplitude and mean brightness, we required monitoring over several epochs, spaced by a month or more. The first epoch was June 2015, and the last was completed in October 2017. Unfortunately, we could not obtain data in October 2015 due to bad weather conditions and we observed a total of 9 epochs.

Observations were taken in the WFC Sloan i and Harris V filters. We selected i band because the spectral energy distribution (SED) of cool evolved stars peaks around 1 μm, thus enhancing the contrast between the LPVs and other, warmer stars. Also, the bolometric correction needed to determine the luminosity in this band is smallest and least dependent on the colour and hence most accurate, and the effects of attenuation by dust are minimal. For monitoring the variations in temperature – and thus radius[1] – and to have more accurate SED modeling, we also observed in V band on several occasions to obtain colour information.

We chose exposure times that yield sufficient signal-to-noise (S/N) to detect small changes in magnitude at different epochs. i band amplitudes of pulsating AGB stars are > 0.1 mag. Therefore, we aimed for $S/N = 10$ for the faintest stars, equivalent to the tip of the RGB. In order to cover the chip gaps of WFC and increase the S/N, the galaxy is observed 9 times with offsets of $30''$ between the pointings each night. Additional observations were made of fields with photometric standard stars to be used for photometric calibration. The details of the observations used in this survey only for And I dwarf galaxy are listed in Table 1.

3   Data processing

The raw images can not be used for scientific analysis before they are combined, calibrated and corrected for artefacts. For this data reduction process, we used THELI (Transforming HEavenly Light into Image), an image processing pipeline for optical images taken by multi-chip (mosaic) CCD cameras [25]. It consists of a number of shell scripts that each perform a specific task and can be run in parallel on multi-chip CCDs. At first, image files are separated into frames of the individual chips (4 CCD chips in a WFC mosaic) and from then on, work is done on individual chips rather than whole images. Next, instrumental signatures

---

[1]Radius R and temperature $T_{\rm eff}$ are related via the luminosity L by the well-known formula $L = 4\pi R^2 \sigma T_{\rm eff}^4$
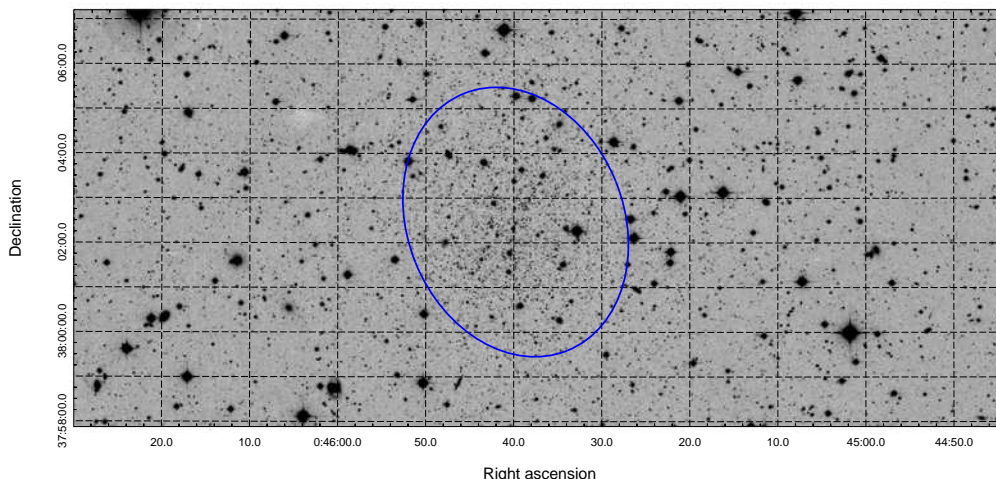
Figure 1: The master WFC image of And I dwarf galaxy. The half-light radii is marked with blue ellipse.

are removed from the data: the electronic offset (bias), pixel response and instrumental throughput variations (flatfield) and interference in the back-illuminated thinned detector chip, especially prevalent at the reddest wavelengths which more closely match the physical thickness of the chip (frigne pattern). While this process is repeated for all of the optical data, the subsequent step strongly depends on the scientific objectives and on the kind of data at hand. The data can be combined, optimised for astrometric accuracy, or optimised for automatised aperture photometry. Because of the crowded nature of the data in the direction of And I itself, it is more important at this stage to obtain accurate astrometry because the photometry will be done based on fitting and subtracting the individual stellar images.

Fortunately, in the THELI pipeline more emphasis is put on precise astrometry than precise photometry and it is perfectly suited to our goal. THELI uses the LDAC (Leiden Data Analysis Center) catalogue format, astronomical object catalogues created by Erik Deul and Emmanuel Bertin [26], and SCAMP package, astrometric tool developed in particular for multi-chip cameras [27], to create a full astrometric solution taking into account the gaps between the chips and overlapping objects. A useful feature of THELI is that it creates weights for individual frames. The weights are created based on the normalized flats. They mask defects such as cosmics and hot pixels in the images. The responsibility of the pipeline ends with the co-addition step. Sky background calculated with the SEXTRACTOR (software for source extraction) package [28] is subtracted from all frames and finally, the SWARP package [29] in THELI creates a co-added image using a weighted mean method [30].

To perform photometry in our crowded stellar field, we used the DAOPHOT/ALLSTAR software developed by Peter Stetson (1987). This package employs a Point Spread Function (PSF) method [31]. After identifying stars (from peaks above the noise) and obtaining aperture photometry for them, about 50–70 isolated stars were chosen in each frame to build an initial PSF model. By subtracting all but the PSF model stars from the frame, a final PSF model was build. Then ALLSTAR subtracts all the stars of image with using PSF fitting photometry along with the current best guesses of their positions and magnitudes.
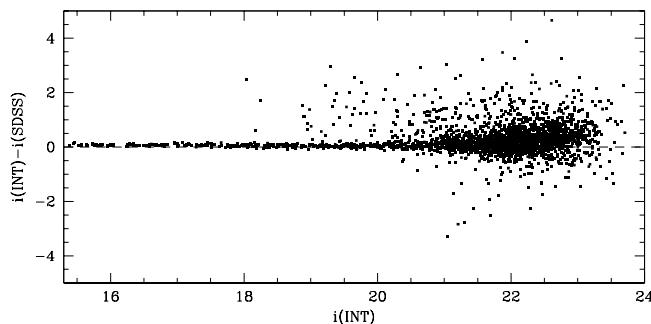
Figure 2: Magnitude differences between INT catalogue and SDSS of And I dwarf galaxy, plotted against i magnitude of our catalogue.

The individual images were aligned using the DAOMASTER routine, which computes the astrometric transformation equation coefficients from the ALLSTAR results. We combined the individual images using the MONTAGE2 routine [32] to create a master mosaic of And I (Fig. 1) and then a master catalogue of stars. This master catalogue was used as input for ALLFRAME, which simultaneously performed PSF-fitting photometry on these stars within each of the individual images. In this way, our final catalogue for And I was made.

To determine aperture corrections to the PSF-fitting photometry, i.e. the difference between the PSF-fitting and large-aperture magnitude of these stars, we used the DAOGROW routine [33]. It constructs growth-curves for each frame from which all stars had been subtracted except the PSF stars. We then applied the COLLECT routine [34] to calculate the aperture correction. We added this value to each of the PSF-fitting magnitudes using the NEWTRIAL routine [35].

Photometric calibration was then performed using the NEWTRIAL routine. Zero points were obtained for each frame based on the standard field observations. To obtain accurate zero points in the Sloan i filter, we applied transformation equations derived from comparing Stetson's compilation of the Landolt standard stars with the corresponding SDSS DR4 photometry [36]. For frames obtained on nights without standard star measurements, we adopted the average of zero points from other nights. Airmass-dependent atmospheric extinction corrections were applied adopting the extinction coefficients determined for La Palma [37].

In order to estimate the accuracy of calibration, we cross correlated the results with the SDSS. The matches were obtained by performing search iterations using growing search radii, in steps of $0.1''$ out to $1''$, on a first-encountered first-associated basis but after ordering the principal photometry in order of diminishing brightness (to avoid rare bright stars being erroneously associated with any of the much larger numbers of faint stars). As shown in Fig. 2, the result is consistent with good accuracy with SDSS catalogue within our desired range ($21 > i > 18$ mag, see below).

4 Quality assessment

To estimate the completeness of our catalogue, we used the ADDSTAR routine in the DAOPHOT package [31]. This task can add synthetic stars to an image, either placed at random by the computer or in accordance with positions and magnitudes specified by us. All photometric are then applied to the new images and so the star-finding efficiency and the photometric
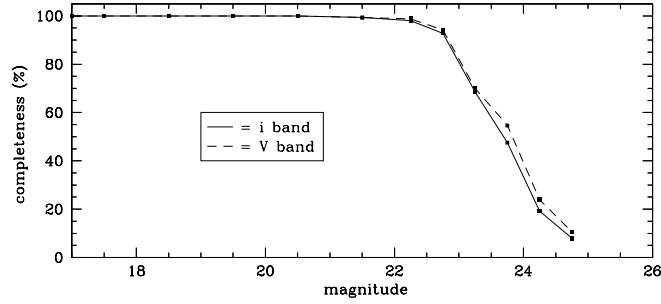
Figure 3: Completeness as a function of i-band (solid line) and V-band (dashed line) magnitude.
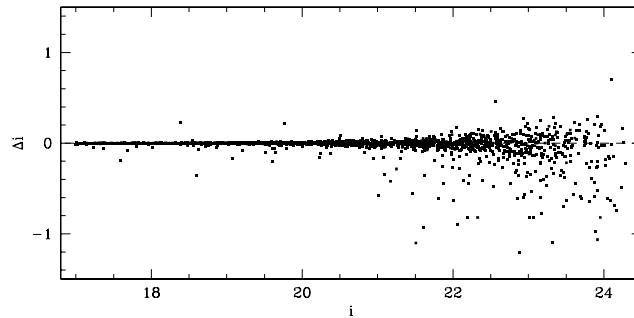

Figure 4: The difference between the input stellar magnitudes and the recovered stellar magnitudes from the artificial star tests.

accuracy can be estimated by comparing the output data for these stars to what was put in.

To avoid small number statistics in the artificial-star analysis without significantly changing the properties of the field (crowdedness), we added 300 artificial stars in each of 8 trials to the master mosaic and two of the individual frames in different bands in 1-mag bins starting from $i = 17$ mag until $i = 25$ mag (for V the same as i). Stars were positioned randomly in the image and Poisson noise was added. Then, we repeated the DAOPHOT/ALLSTAR/ALLFRAME procedure on the new frames as described before. Once the photometry was done and the final list created, we used DAOMASTER to evaluate what fraction of stars was recovered. As one can see in Fig. 3, our catalogue is essentially complete down to $i \sim 22$ mag (near the RGB–tip, see below), dropping to below 50% at $i = 23.6$ mag. The V-band reaches similar completeness levels but at ~ 0.1 magnitude fainter.

The result of estimating the accuracy of our photometry is shown in Fig. 4. The difference between the input stellar magnitudes and the recovered magnitudes down to $i \sim 22$ mag is very small, $|\Delta i| < 0.1$ mag, but it increases for fainter magnitudes. So, this photometry is deep enough to meet the scientific objectives of our project of studying AGB stars and RSGs, because they have $i < 21.5$ mag – except possibly for heavily dust-enshrouded cases, which however are rare.
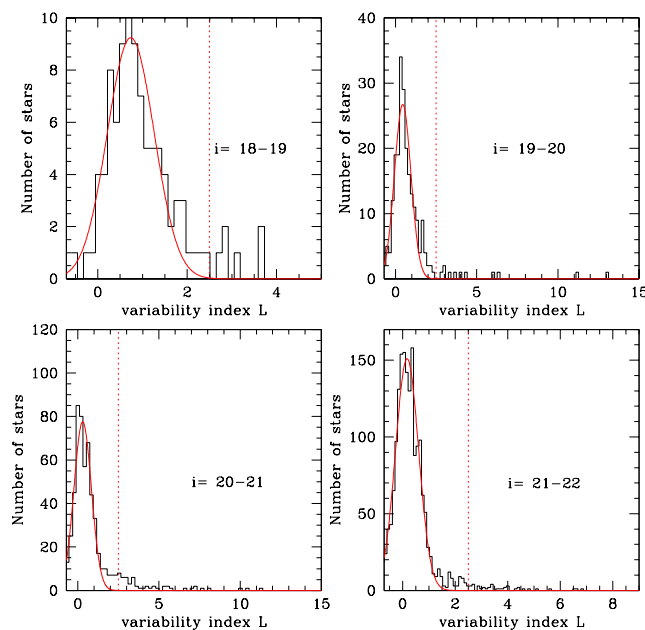
Figure 5: Histograms of the variability index L, for several i-band magnitude bins. The solid lines show Gaussian functions fitted to the histograms.

5 Variability analysis

For finding variable star candidates, we used the NEWTRIAL program [34]. This program was introduced by Welsh & Stetson (1993) and developed further by Stetson (1996). In this method, the observations are paired on the basis of timespan between observations such that the observations of each pair have a timespan less than the shortest period expected for the kind of the variable stars of interest (100 days or longer for LPVs). If within a pair of observations only one measurement is available for a particular star then the weight of the pair for that star is set to 0.5.

The NEWTRIAL program first calculates the J index:

$$J = \frac{\Sigma_{k=1}^{N} w_k \ \mathrm{sign}(P_k)\sqrt{|P_k|}}{\Sigma_{k=1}^{N} w_k}. \tag{1}$$

Here, observations i and j have been paired and each pair k has been given a weight w_k; the product of the normalized residuals, $P_k = (\delta_i \delta_j)_k$, where $\delta_i = (m_i - \langle m \rangle)/\epsilon_i$ is the deviation of measurement i from the mean, normalized by the error on the measurement, ϵ_i. Note that δ_i and δ_j may refer to measurements taken in different filters ($P_k = \delta^2 - 1$ if $i = j$). The J index has a large positive value for variable stars and tends to zero for data containing random noise only.

When we are dealing with a small number of observations or corrupt data we gain from also calculating the Kurtosis index:

$$K = \frac{\frac{1}{N}\Sigma_{i=1}^{N}|\delta_i|}{\sqrt{\frac{1}{N}\Sigma_{i=1}^{N}\delta_i^2}}. \tag{2}$$
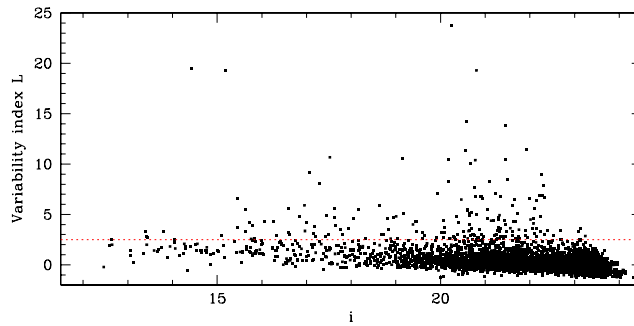
Figure 6: Variability index L *vs.* i-band magnitude. The dashed line indicates our threshold for identifying variable stars, at $L > 2.5$.

The value of K depends on the shape of the light-curve: $K = 0.9$ for a sinusoidal light variation, where the source spends most time near the extrema, $K = 0.798$ for a Gaussian distribution, which is concentrated towards the average brightness level (as would random noise), and $K \to 0$ for data affected by a single outlier (when $N \to \infty$).

Also, there is a variability index that depends on both the J and K indices [35]:

$$L = \frac{J \times K}{0.798} \frac{\Sigma_{i=1}^{N} w_i}{w_{\text{all}}}, \tag{3}$$

where Σw is the total weight assigned to a given star and w_{all} is the total weight a star would have if observed in every single observation. We used L variability index for finding variable stars in this paper. One reason for using it is that the lightcurves of LPVs have shapes roughly between sinusoidal and triangular, and thus a kurtosis near 0.9-1. The L index is weighted by that kurtosis, making it larger for such variations compared to more random or erratic variations.

To determine the optimal variability threshold, we plotted histograms of the variability index for several i-band magnitude intervals in the range 18–22 mag along with a fitted Gaussian function to each of them. As shown in Fig. 5, while the Gaussian function is a near-perfect fit to the symmetrical distributions at low values for L, the distributions show a pronounced tail towards higher values for L. The departure from the Gaussian shape occurs typically around $L \approx 2.5$. Fig. 6 shows how the variability index L varies with i-band magnitude. The dashed line indicates our threshold for detected variability: $L > 2.5$.

The number of variable stars are suspect and we inspected all of the stars by eye. Some of these stars are located near the edge of the frame and some others located on the site of a saturated star in image, resulting in particularly poor photometry on several epochs with distorted stellar profiles and therefore, they are unreliable. We removed these stars and thus identified 116 variable stars in the And I. Two examples of likely long-period variability are shown in Fig. 7, with a non-variable star for comparison. One of the variable stars was also found to be variable at mid-IR wavelengths in the *Spitzer* monitoring survey DUSTiNGS [38] (cf. Section 6).

5.1   Amplitudes of variability

A measure for the amplitude of variability can be obtained by assuming a sinusoidal light-curve shape. It is done by comparing the standard deviation in the magnitudes to that
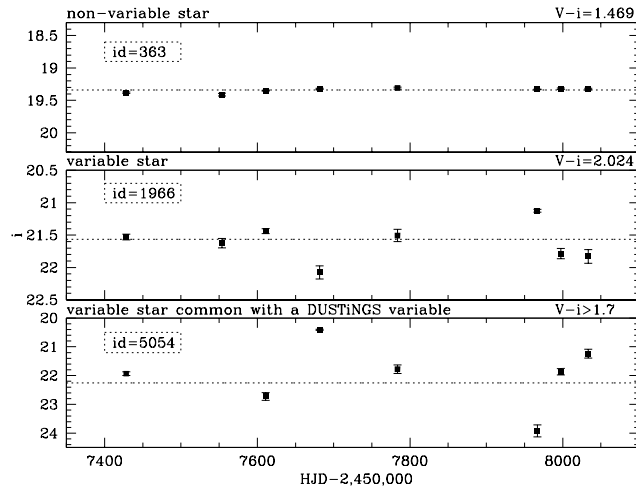
Figure 7: Example light-curves of two variable stars, with #5054 in common with the DUSTiNGS catalogue of variable *Spitzer* sources [38], with a non-variable star in the top panel for comparison.
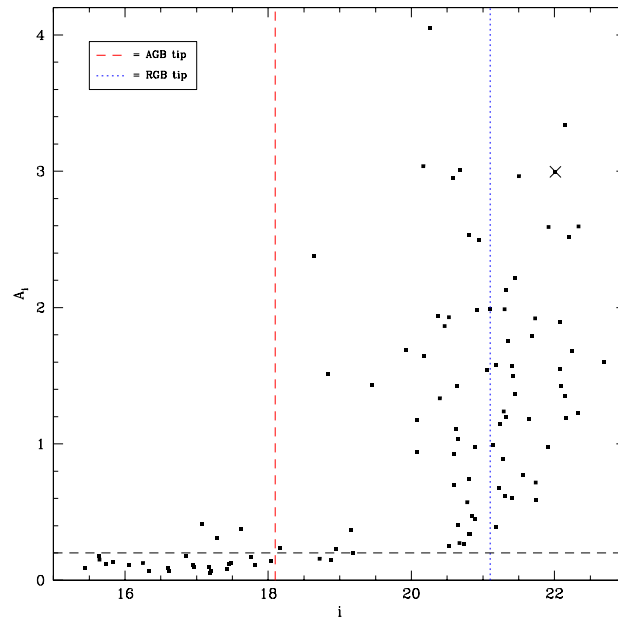

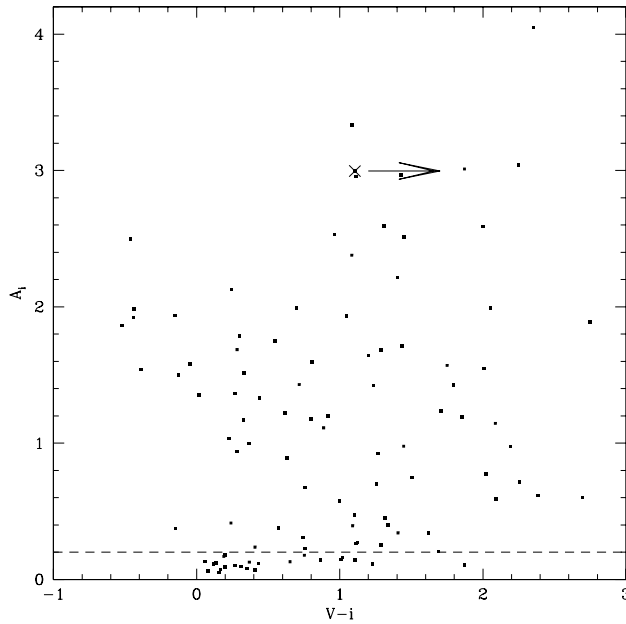Figure 8: Estimated amplitude, A_i, of variability *vs. i*-band magnitude.

Figure 9: Estimated amplitude, A_i, of variability *vs.* colour.

expected for a completely random sampling of a sinusoidal variation. The estimated i-band amplitude of variability is plotted *vs.* i-band magnitude in Fig. 8. Variability could have been detected for $A_i > 0.2$ mag. There is a clear tendency for the amplitude to diminish with increasing brightness, which is a known [39, 40, 41] and to some extent understood [42] trend for AGB stars. The amplitudes stay below $A_i \sim 4.2$ mag and generally $A_i < 2.5$ mag. Very dusty AGB stars are known to reach such large amplitudes [39, 40, 41], but they are very rare. One example of such star, #5054 is highlighted in Fig. 8 with a cross; its lightcurve is displayed in Fig. 7 and it was also identified as a mid-IR variable by the DUSTiNGS survey [38]. The most interesting stars might be those three brighter than the tip of the AGB and with amplitude about 0.3–0.4 mag. They could be very massive AGB stars undergoing Hot Bottom Burning or RSGs and therefore, represent a "young" population (< 100 Myr).

The estimated i-band amplitude of variability is plotted *vs.* the $V - i$ colour in Fig. 9. Stars towards redder colours have larger amplitudes. This is not surprising as large-amplitude variability is known to be associated with abundant dust formation [39, 40, 41]. For the DUSTiNGS variable (#5054), we estimated $V > 23.7$ and thus $(V - i) > 1.7$ due to the completeness limit in V-band (23.7 mag).

6   Discussion

Our final catalogue contains 10585 stars in the region of CCD 4 of WFC (11.26×22.55 arcmin^2), with And I located near its center. Fig. 10 presents the spatial location of our variable candidates. The half-light radii is marked with a blue ellipse. The density of variable stars for the regions inside and outside the ellipse are 0.68 and 0.43 number/arcmin^2, respectively.

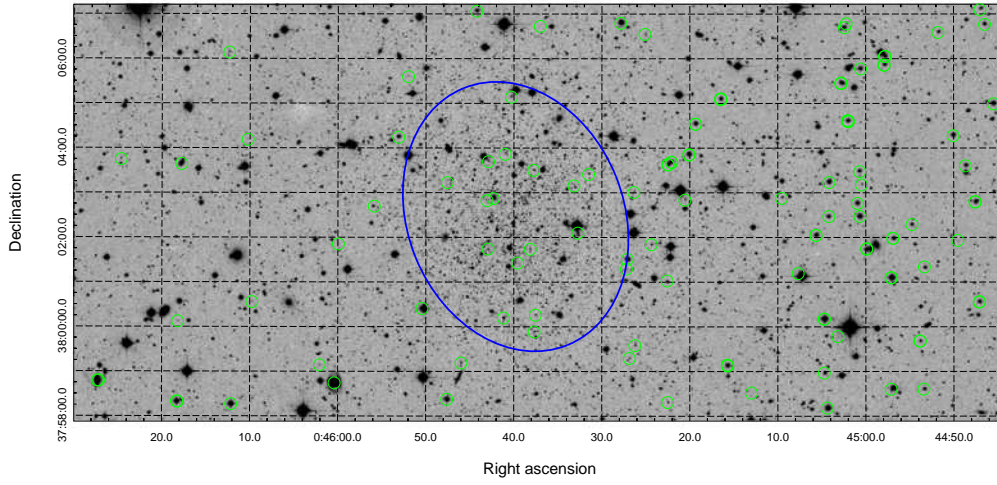Colour–magnitude diagrams of this galaxy in i-band and V-band *vs.* $(V - i)$ colour are

Figure 10: The master WFC image of And I dwarf galaxy with spatial location of our variable candidates. The half-light radii is marked with blue ellipse.
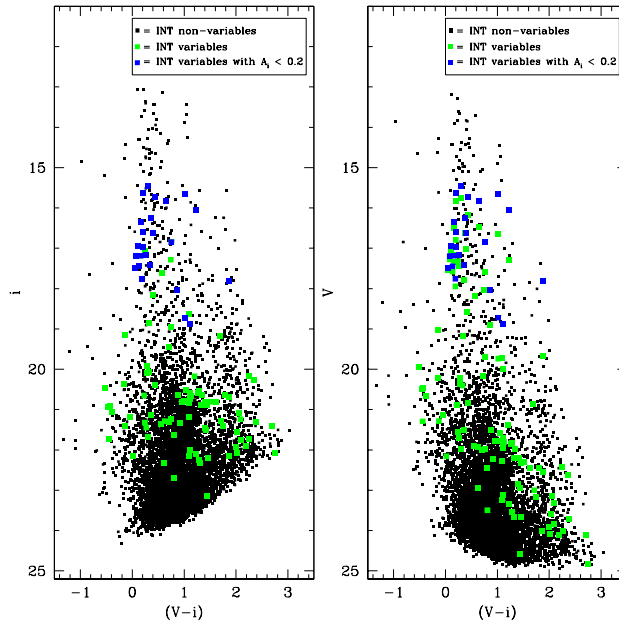

Figure 11: colour–magnitude diagrams showing the variable stars in green. The variable stars with $A_i < 0.2$ mag are highlighted in blue.
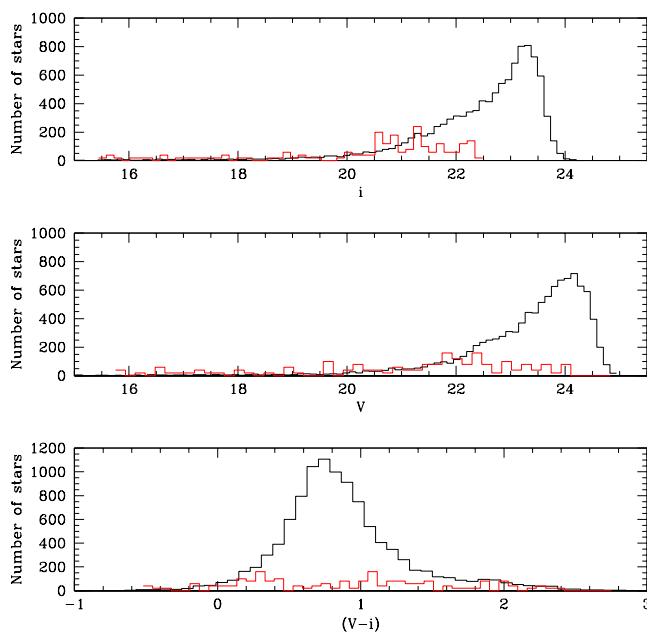
Figure 12: Distribution of all INT sources (black) and INT variable stars (red) as a function of brightness and colour. we multiplied the variable stars' histograms by 20.

shown in Fig. 11. The variable stars we identified are highlighted in green. These are mainly found between $i \sim 18$–22 mag, and as the stars get fainter, their number decreases. Some brighter variable RSGs are found (around $i \sim 16$–18 mag), too.

Fig. 12 presents histograms of the distributions over brightness and colour. The largest fraction of stars that are found to be variable occurs between $i \sim 18$–22 mag. As the frequency of stars increases from $i \sim 22$ mag, the frequency of variable stars decreases. This is probably because many stars have not yet reached the final phase of their evolution and they will still evolve to higher luminosities and lower temperatures before they develop large-amplitude variability.

To assess the level of contamination by foreground stars, we performed a simulation with the TRILEGAL tool [43]. We simulated two different sizes of the field, a 0.07 deg^2 (about the size of the entire CCD4 of WFC) and a 0.007 deg^2 (half the light of the galaxy), in the direction ($l = 121.68°$, $b = -24.82°$). As shown in Fig. 13 the foreground stars have contaminated our desired areas; therefore, the distribution of the population of AGB stars and then the star formation history can not be obtained from colour–magnitude diagrams alone. Because LPVs are relatively rare, and become rare still in directions away from the Galactic plane, one could instead use the distributions over LPVs to chart the star formation history, relatively free from foreground contamination.

The stellar population in the And I dwarf galaxy can be described using isochrones calculated by Marigo et al. (2008) (Fig. 14) [44]. The isochrones were calculated for And I metallicity, $Z = 0.00069$ [20]. The 100-Myr and 1-Gyr isochrones show consistency with the red branch of INT variables. The 10-Gyr isochrone defines the location of tip of the RGB, that here is 21.1 mag for i band. These isochrones are the most appropriate theoretical models for our purpose, for the following reasons:
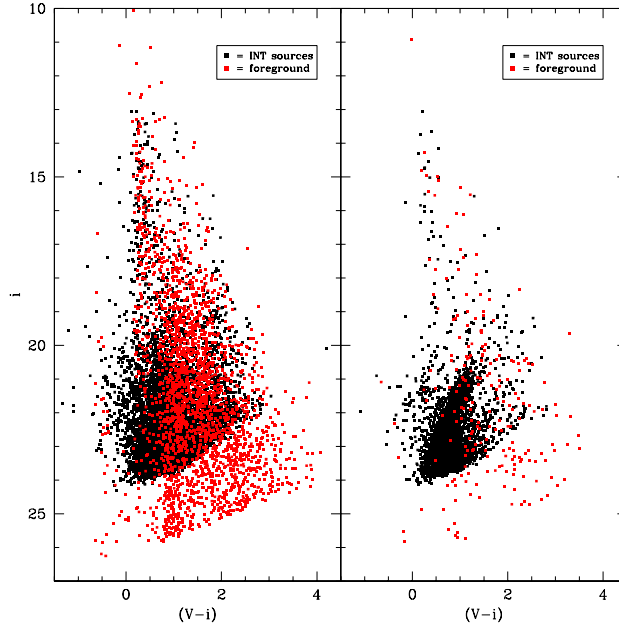
Figure 13: Estimated contamination by foreground stars (in red), from a simulation with TRILEGAL [43]. In the left panel, a 0.07 deg^2 field is considered while in the right panel, we have a 0.007 deg^2 field centered on And I (half the light of the galaxy).
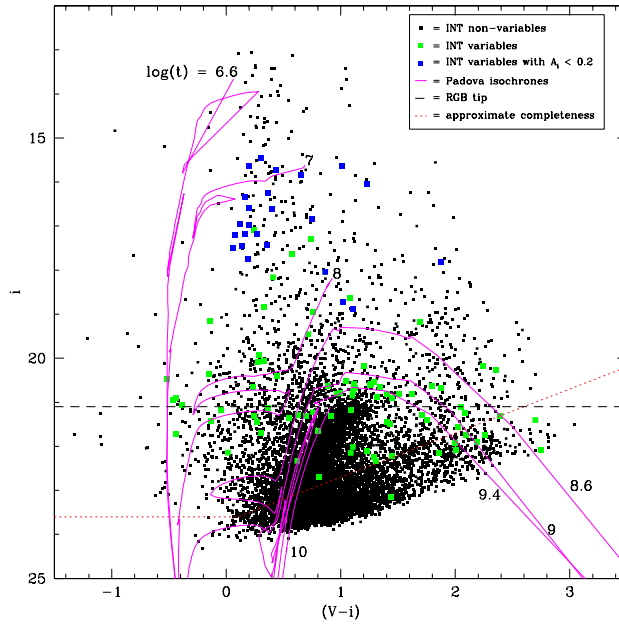

Figure 14: colour–magnitude diagram of $(V - i)$, with variable stars highlighted in green. The variable stars with $A_i < 0.2$ mag are highlighted in blue. Overplotted are isochrones from Marigo et al. (2008) for And I with a distance modulus of 24.49 mag [23].

- The star's evolution is followed all the way through the thermal pulsing AGB until the post-AGB phase. Crucially, two important phases of stellar evolution are included, viz. the third dredge-up mixing of the stellar mantle as a result of the helium-shell burning phase, and the enhanced luminosity of massive AGB stars undergoing hot bottom burning (HBB) [45];

- The molecular opacities which are important for the cool atmospheres of evolved stars have been considered in the models of stellar structure. The transformation from oxygen-dominated (M-type) AGB stars to carbon stars in the birth mass range $M \sim$ 1.5–4 M$_\odot$ is accounted for [46];

- The dust production in the winds of LPVs, and the associated reddening is included;

- The radial pulsation mode is predicted;

- Combination of their own models for intermediate-mass stars ($M < 7$ M$_\odot$), with Padova models for more massive stars ($M > 7$ M$_\odot$ [47]), gives a complete coverage in birth mass ($0.8 < M < 30$ M$_\odot$);

- Magnitudes are calculated on a wide range of common optical and IR photometric systems;

- The isochrones are available via an internet-based form in a user-friendly format.

6.1   Cross-identifications in other catalogues

We cross-correlate our INT variability search results with the mid-IR variability search performed with the *Spitzer* Space Telescope [11] and also, with the variables catalogue obtained with the *Hubble* Space Telescope (HST) data [23]. The matches were obtained by search iterations using growing search radii, in steps of $0.1''$ out to $1''$, on a first-encountered first-associated basis after ordering the principal photometry in order of diminishing brightness (i-band/I-band for the optical catalogues, and 3.6-μm band for the *Spitzer* catalogue).

DUSTiNGS (DUST in Nearby Galaxies with *Spitzer*) was a 3.6 and 4.5 μm post-cryogen *Spitzer* Space Telescope imaging survey of 50 dwarf galaxies within 1.5 Mpc that was designed to identify dust-producing AGB stars and massive stars [11]. Using 2 epochs, spaced approximately 6 months apart, they identified a total of 4 variable stars for And I. As a result of cross-correlating, we obtained 5616 common stellar sources between our photometric catalogue and the DUSTiNGS survey in a 0.07 square degree field centered on And I. As shown in Fig. 15, all four of their variable stars are listed in our identified variables catalogue. We found a few variables among the brighter red giants, including a red one, at $[3.6] - [4.5] = 1$ mag. We did not find variables above the tip of the 10 million year isochrone, which is consistent with there being no LPVs among stars more massive than those which become RSGs. Also we did not find variables among the redder sources, $[3.6] - [4.5] > 0.4$ mag, around $[3.6] \sim 17 - 18$ mag. Is it possible that these sources have only been detected in our survey in one epoch, when they were near maximum brightness, so we could not determine any variability.

Martínez-Vázquez et al. (2017) presented the ISLAndS (Initial Star formation and Lifetimes of Andromeda Satellites) project, providing a census of variable stars in six M31 dSph satellites observed with the HST. They detected 296 RR Lyrae stars in And I [23]. There are 59 objects in common between their survey and ours, among which only two were identified by us as variable (Fig. 16). This illustrates that these surveys probe entirely different, complementary populations – the oldest populations (ISLAndS) and the intermediate-age and younger populations (our survey).
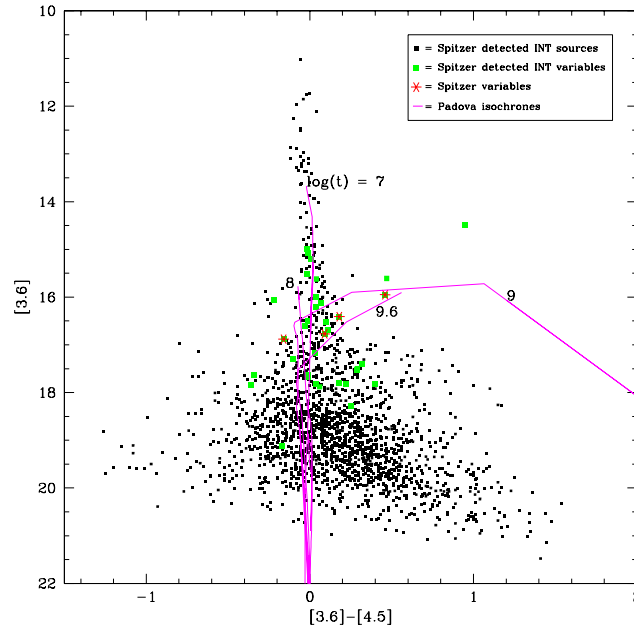
Figure 15: Mid-IR colour–magnitude diagram from DUSTiNGS survey, with INT variables highlighted in green and the variable stars of DUSTiNGS in red asterices. Isochrones from Marigo et al. (2008) for 10 Myr, 100 Myr 1 Gyr and 4 Gyr are drawn.
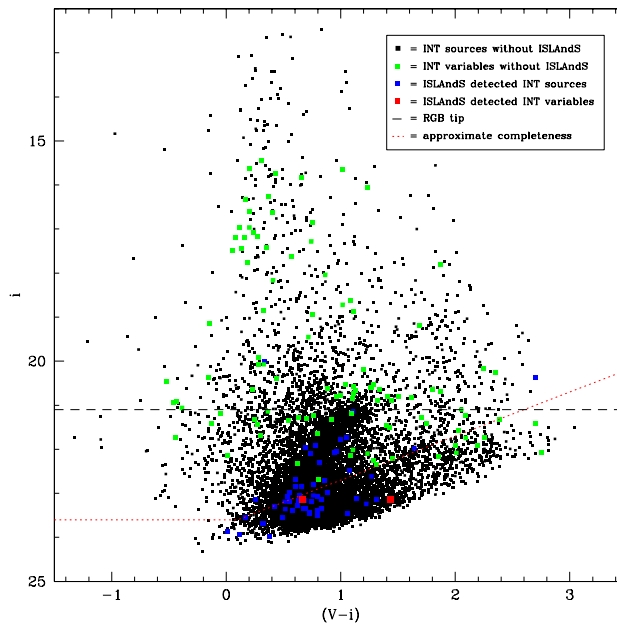

Figure 16: Optical colour–magnitude diagram showing the stars from the INT survey that were and were not detected in the ISLAndS variability survey [23]. Two red points represent common variable stars between the two surveys.

7 Conclusions

We have presented the preliminary, initial results from our long-term optical monitoring campaign at the Isaac Newton Telescope of a sample of the LG dwarf galaxies, namely for the And I satellite of M31. We found 116 variable stars, including a few among the brighter and redder sources, some of which have also been detected at mid-IR wavelengths. This indicates the presence of stars around a Gyr or younger in And I, which contribute to the replensihment of the interstellar medium within And I.

Acknowledgments

References

[1] Mateo M., Olszewski E. W., Vogt S. S., Keane M. J., 1998, AJ, 116, 2315

[2] Kleyna J. T., Wilkinson M. I., Evans N. W., Gilmore G., 2004, MNRAS, 354, L66

[3] Gilmore G., et al., 2007, ApJ, 663, 948

[4] Walker M. G., Mateo M., Olszewski E. W., Peñarrubia J., Evans N.W., Gilmore G. 2009, ApJ, 704, 1274

[5] Wolf J., et al., 2010, MNRAS, 406, 1220

[6] Dolphin A. E., Weisz D. R., Skillman E. D., Holtzman J. A., 2005, ASP Conference Series

[7] Read J. I., Pontzen A. P., Viel M., 2006, MNRAS, 371, 885

[8] Tolstoy E., Hill V., Tosi M., 2009, ARA&A, 47, 371

[9] Weisz D. R., et al., 2011, ApJ, 743, 8

[10] Kazantzidis S., Lokas E. L., Mayer L., Knebe A., Klimentowski J., 2011, ApJL, 740, L24

[11] Boyer M. L., et al., 2015, ApJ, 216, 10

[12] Saremi E., et al., 2017, J. Phys.: Conf. Ser, 869, 012068

[13] Javadi A., van Loon J. Th., Mirtorabi M. T., 2011a, MNRAS, 411, 263

[14] Rezaeikh S., Javadi A., Khosroshahi H., van Loon J. Th., 2014, MNRAS, 445, 2214

[15] Javadi A., et al., 2015, MNRAS, 447, 3973

[16] Javadi A., van Loon J. Th., Khosroshahi H., Tabatabaei F., Golshan R. H., 2017, MNRAS, 464, 2103

[17] Golshan R. H., Javadi A., van Loon J. Th., Khosroshahi H., Saremi E., 2017, MNRAS, 466, 1764

[18] McConnachie A. W., Irwin M. J., 2006, MNRAS, 365, 1263

[19] Da Costa G. S., Armandroff T. E., Caldwell N., Seitzer P., 1996, AJ, 112, 2576

[20] Kalirai J. S., et al., 2010, ApJ, 711, 671

[21] Martin N. F., et al., in press (arXiv:1704.01586)

[22] McConnachie A. W., et al., 2004, MNRAS, 350, 243

[23] Martínez-Vázquez., et al., in press (arXiv:1710.09038)

[24] Conn A. R., et al., 2012, ApJ, 758, 1

[25] Erben T., et al., 2005, AN, 326, 432

[26] E.Deul, ftp://ftp.strw.leidenuniv.nl/pub/ldac/software/

[27] Bertin E., 2006, ADASS XV: ASP Conf. Ser, 351, 112

[28] Bertin E., Arnouts S., 1996, A&A Supplement, 117, 393

[29] Bertin E., 2010, Astrophysics Source Code Library, 10068

[30] Schirmer M., 2013, ApJ Supplement, 209, 2

[31] Stetson P. B., 1987, PASP, 99, 191

[32] Stetson P. B., 1994, PASP, 106, 250

[33] Stetson P. B., 1990, PASP, 102, 932

[34] Stetson P. B., 1993, in: Stellar Photometry Current Techniques and Future Developments, IAU Coll. Ser. 136, 291

[35] Stetson P. B., 1996, PASP, 108, 851

[36] Jordi K., Grebel E. K., Ammon K., 2006, A&A, 460, 339

[37] García-Gil A., Muñoz-Tuñón C., Varela A. M., 2010, PASP, 122, 1109

[38] Boyer M. L., et al., 2015 ApJ, 800, 51

[39] Wood P. R., Whiteoak J. B., Hughes S. M. G., Bessell M. S., Gardner F. F., Hyland A. R., 1992, ApJ, 397, 552

[40] Wood P. R., 1998, A&A, 338, 592

[41] Whitelock P. A., Feast M. W., van Loon J. Th., Zijlstra A. A., 2003, MNRAS, 342, 86

[42] van Loon J. Th., et al., 2008, A&A, 487, 1055

[43] Girardi L., Groenewegen M. A. T., Hatziminaoglou E., da Costa L., 2005, A&A, 436, 895

[44] Marigo P., Girardi L., Bressan A., Groenewegen M. A. T., Silva L., Granato G. L., 2008, A&A, 482, 883

[45] Iben I. Jr., Renzini A., 1983, ARA&A, 21, 271

[46] Marigo P., Girardi L., 2007, A&A, 469, 239

[47] Bertelli G., Bressan A., Chiosi C., Fagotto F., Nasi E., 1994, A&A, 106, 275

A Simplified Solution for Advection Dominated Accretion Flows with Outflow

Seyede Tahere Kashfi · Shahram Abbassi

Department of Physics, Ferdowsi University of Mashhad, Mashhad, Iran

Abstract. The existence of outflow in the advection dominated accretion flows has been confirmed by both numerical simulations and observations. The outflow models for ADAF have been investigated by several groups with a simple self similar solution. But this solution is inaccurate at the inner regions and can not explain the emitted spectrum of the flow; so, it is necessary to obtain a global solution for ADAFs with outflow. In this paper, we use a simplified global solution to study the structure of ADAF in the presence of outflow. In this method which is proposed by Yuan et al (2008, hereafter YMN08), the radial momentum equation is replaced by a simple algebraic relation between angular velocity and Keplerian angular velocity to avoid the difficulty of the calculation of global solution. We consider the radial dependence for mass accretion rate $\dot{M} = \dot{M}_{out}(r/r_{out})^s$ where s is a constant and we do not change the other dynamical equations. We investigate the variation of physical quantity of accretion flow which is caused by outflow. The results that we obtained comply with our expectations from the influence of outflow on the structure of accretion flow.

Keywords: accretion; accretion disks; black hole; global solution; outflow

1 Introduction

Advection dominated accretion flow (ADAF) is an important model for black hole accretion. In this model which is introduced by Narayen & Yi (1994, Abramowicz et al. 1995, Chen et al. 1995), most of the energy is stored in the accretion gas and advected to the central black hole. The ADAFs have high temperature and thermal stability and can explain the hard X-ray emission from X-ray sources and AGNs. Also, because the advective nature of these flows, they are especially good to explaining low luminous systems.

On the one hand, as Narayan & Yi (1994, 1995a) noted, this type of accretion flow have an interesting feature that is the positive value for Bernoulli parameter. This parameter is the sum of the gravitational potential energy, kinetic energy and the enthalpy of the flow. When this parameter have a positive value, the gas can escape to infinity, and on the another hand, for a given density at a large distance from the black hole (e.g., measured by Chandra on $1''$ scales), the density close to the black hole is much less than the ADAF or Bondi prediction (Yuan et al. 2003). Also, numerical simulations (Stone et al. 1999; Hawley & Balbus 2002; Igumenshchev et al. 2003) indicate that a large fraction of accretion material of the flow can not reach the central black hole and it is lost in the form of outflow. For these reasons, the existence of outflows should be considered in ADAF models.

Outflow models for ADAF have been investigated by several group (Xu & Chen 1997; Blandford & Begelman 1999; Beckert 2000; Xue & Wang 2005; Bu et al. 2009), in the frame of a self similar solution. Self similar solution is only valid for the regions away from the boundaries and does not match the boundary conditions of the flow; also, it is too simplified for calculating the emitted spectrum; so, we need to obtain the global solution.

Quataert & Narayan (1999) presented the global solution for ADAF with outflow for the first time. They use the form $\dot{M} \propto r^s$ to describe the accretion rate. In their investigation, all dynamical equations of the flow do not change, except the continuity equation. They calculated spectral models of ADAFs with outflow and compared their results with observations of several astrophysical systems. Also, Yuan et al. (2003; 2009) adopted the same approach for RIAFs and hot accretion flows.

However, the global solution is a two points boundary value problem and technically, it is difficult to solve. Because the difficulty of calculating the global solution, the effect of existence of outflow on the structure of ADAFs has not been investigated any more.

In this paper, we focus on the structure of ADAFs in the presence of outflow rather than the calculation of the emitted spectrum. By following the simplified global solution which is introduced by YMN08, we replace the radial momentum equation by a simple algebraic relation between the angular velocity and Keplerian angular velocity of the flow. In this way, we avoid the two points boundary value problem and the consequently, the approximate global solution for ADAF with outflow can be obtained.

We present the basic equations in section 2, and numerical results in section 3. Section 4 is devoted to a short summary. We should note that the effect of outflow on the angular momentum and energy equations is ignored here. Since the most important effect of outflow is to modify the density profile, we do not expect this treatment to cause a remarkable change on our results.

2 Basic Equations

We consider an advection dominated accretion flow which is axisymmetric and steady state ($\frac{\partial}{\partial t} = \frac{\partial}{\partial \varphi} = 0$). The Paczyński & Witta potential $\phi = -\frac{GM}{(r-r_g)}$ is adopted to mimic the geometry of a Schwarzschild black hole where M is the mass of black hole and $r_g = \frac{2GM}{c^2}$ is the Schwarzschild radius. Also, the hydrostatic equilibrium in the vertical direction is assumed; so, we have a heghit-integrated set of equations. In this formulation, all physical quantities are functions of only the cylindrical radius.

To take into account the role of outflow, the continuity equation must be modified. So, we consider the dependency of the mass accretion rate on radius as follows (Blandford & Begelman 1999)

$$\dot{M} = -4\pi r \rho H v_r = \dot{M}_{out}(\frac{r}{r_{out}})^s \tag{1}$$

where $\dot{M}_{out}$ is the mass accretion rate at the outer radius and s is a parameter that indicates the strength of outflow. All the other quantities have their usual meanings.

The other equations that describe the structure of flow are

$$v_r \frac{dv_r}{dr} = (\Omega^2 - \Omega_K^2)r - \frac{1}{\rho}\frac{dp}{dr}, \tag{2}$$

$$v_r(\Omega r^2 - j) = -\alpha r c_s^2, \tag{3}$$

$$\rho v_r(\frac{d\epsilon_i}{dr} - \frac{p_i}{\rho^2}\frac{d\rho}{dr}) = (1-\delta)q^+ - q_{ie}, \tag{4}$$

$$\rho v_r(\frac{d\epsilon_e}{dr} - \frac{p_e}{\rho^2}\frac{d\rho}{dr}) = \delta q^+ + q_{ie} - q^-. \tag{5}$$

In these equations, $\epsilon_i(\epsilon_e)$ is the internal energy of ions (electrons) per unit mass of gas and $p_i(p_e)$ is the pressure due to ions (electrons) which is defined as

$$\epsilon_e = \frac{1}{\gamma_e - 1}\frac{kT_e}{\mu_e m_H}, \qquad \epsilon_i = \frac{1}{\gamma_i - 1}\frac{kT_i}{\mu_i m_H}, \tag{6}$$

$$p_i = \frac{\rho}{\mu_i}\frac{k}{m_H}T_i, \qquad p_e = \frac{\rho}{\mu_e}\frac{k}{m_H}T_e \tag{7}$$

The q^+ is the net turbulent heating rate and the quantity δ determines the fraction heating rate that directly heats electrons. q_{ie} describes the energy transfer rate from ions to electrons by Coulomb collision and q^- is the radiative cooling rate that includes bremsstrahlung and synchrotron emission and their Comptonization (see Manmoto et al. 1997 for detail).

The set of dynamical equations includes two algebraic equations (1) and (3) and three first order differential equations (2), (4) and (5). To solve these differential equations we need to have the outer boundary conditions for v_r, T_i and T_e. Also, because the transonic nature of ADAF, the sonic point conditions have to be considered and the most difficult part of this solution is to apply these conditions in the radial momentum equation.

By following YMN08, we use a simple relation between angular velocity and Keplerian angular velocity;

$$\Omega = f\Omega_k \tag{8}$$

where

$$f = \begin{cases} f_0 & r > 3r_g \\ 3f_0\frac{r-r_g}{2r_g} & r < 3r_g. \end{cases}$$

In this relation, f_0 is an adjustable parameter that YMN08 defined it as $f_0 = 0.33$ for a wide rang of $\dot{M}$ and a large value of α.

With considering this simple relation, the radial velocity become

$$v_r = \frac{-\alpha r c_s^2}{(f\Omega_k r^2 - j)}. \tag{9}$$

By substituting the equations (1) and (9) into the energy equations and expressing the isothermal sound speed c_s in terms of ions and electrons temperature, we can obtain two first order differential equations for two unknown variables T_i and T_e. If we have T_i and T_e at the outer boundary, we can integrate these differential equations inward for a given value of α and $\dot{M}$. The other physical quantities such as ρ, v_r and c_s will be calculated from the relations which they have with temperature. We use the the standard fourth order Runge-Kutta method and solve the differential equations with initial conditions.

3   Results

In our calculations, we set $M = 10M_\odot$ and $\delta = 0.3$. We examine our approach for different values of s, α and $\dot{M}$. The conditions that we imposed at the outer boundary are the same as in YMN08.

Figure 1 shows the variation of the accretion rate as a function of radius for $s = 0$, $s = 0.2$, $s = 0.4$ and $s = 0.6$. In this figure, the solid line indicates the case without outflow. In the presence of outflow, as radius decreases, the accretion rate declines and for a powerful outflow $s = 0.6$, only a few of material can be accreted on the black hole.
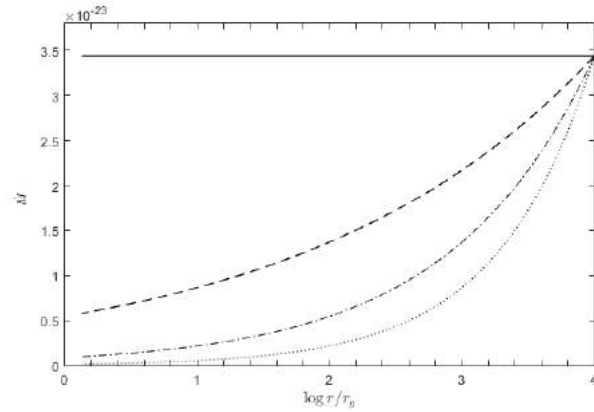
Figure 1: Accretion rate as a function of radius. The solid line, dashed line, dash dotted line and dotted line are related to $s = 0$, $s = 0.2$, $s = 0.4$ and $s = 0.6$ respectively.

Figure 2 indicates the radial variation of cooling rate. q^- includes three radiation mechanisms, bremsstrahlung radiation, synchrotron radiation and their Comptonization. In the outer regions of the flow, the bremsstrahlung emission is dominated while the synchrotron and Comptonization are the main emissions in the hot inner regions [8]. The bremsstrahlung emission is almost insensitive to the existence of outflow. As the figure 2 demonstrates, the cooling rate in the outer radii dose not change with the increasing the value of s because in these regions, the bremsstrahlung radiation is important and the effects of synchrotron and Comptonization emissions are negligible.

From the studies on the emitted spectrum [12], we know that the synchrotron emission decreases strongly with increasing s because when the value of s increases, the density and gas pressure decrease, so it is produced a weaker magnetic field. With increasing s the Compton power decreases strongly more than the synchrotron. In figure 2, we can see that the total cooling rate significantly reduces with large value for s.
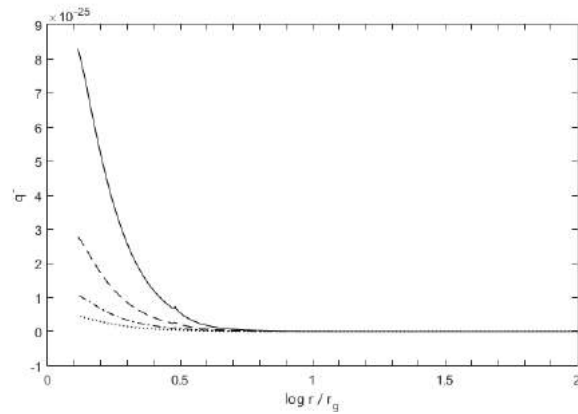

Figure 2

In figures 3 and 4, the profiles of ions and electrons temperature, radial velocity and density for different values of α and $\dot{M}$, are shown. In figure 3, $\alpha = 0.1$ and $\dot{M}_{out} =$

$10^{-3}\dot{M}_{Edd}$, and in figure 4, $\alpha = 0.3$ and $\dot{M}_{out} = 10^{-3}\dot{M}_{Edd}$. In figure 3, the radius of outer boundary is $r_{out} = 10^4 r_g$ and boundary conditions are $T_i = 0.2T_{vir}$, $T_e = 0.19T_{vir}$ where $T_{vir} = 3.6 \times 10^{12}(\frac{r_g}{r})$.

As we expected, the profile of density indicates an obvious decline in the presence of outflow. When $s = 0.6$, the value of density in the inner radii is almost 10^2 times less than the case without outflow. Also, the radial velocity decreases with increasing the value of s. In the profile of radial velocity, the variation of sound speed with radius is illustrated too. By comparing the profiles related to different value of s, we can realize that as s increases, the sonic point moves in and comes close to the black hole.

The plot of ions temperature shows that when s increases, the ions temperature decreases. From equation (4), we know there are two terms that affect the value of T_i, q^+ and q_{ie} and from their definitions, we know $q^+ \propto \dot{M}$ and $q_{ie} \propto \dot{M}^2$. Therefore, when the outflow exists, these two terms decrease and reduce the ions temperature.

In the outer regions of the electrons temperature profile, there is a decline in temperature when s increases. As we mentioned before, in these radii, the bremsstrahlung radiation dominates and this radiation is unaffected by the outflow. By return to the energy equation for electrons, we can see if q^- dose not change very much, the variation of two other terms q^+ and q_{ie} reduces the electrons temperature because they are the heating processes for electrons and with increasing s, these terms decrease. By contrast, in the inner radii, the cooling rate strongly decreases and this causes an increasing in electrons temperature. So, for the region close to the black hole, we have a larger T_e.
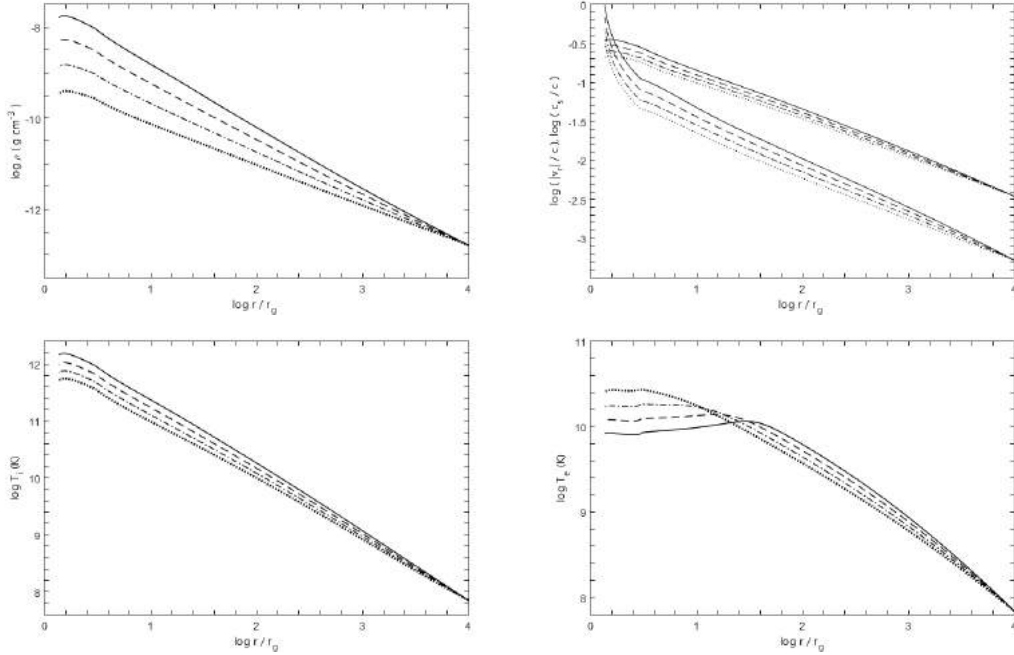

Figure 3: The variations with radii of density, radial velocity, ions temperature and electrons temperature for $s = 0$, $s = 0.2$, $s = 0.4$ and $s = 0.6$ are represented by solid, dashed, dash dotted and dotted lines respectively. The outer boundary is set at $10^4 r_g$ with the boundary conditions of $T_i = 0.2T_{vir}$ and $T_e = 0.19T_{vir}$ and $\alpha = 0.1$ and $\dot{M}_{out} = 10^{-3}\dot{M}_{edd}$ are fixed.

Figure 4 shows the variations of physical quantities in the presence of outflow for an

another case. In this figure, the outer radius is $r_{out} = 10^2 r_g$ and boundary conditions are $T_i = 0.6T_{vir}$ and $T_e = 0.08T_{vir}$. The parameters α and $\dot{M}_{out}$ have a larger value in comparison with the case that was discussed in figure 3. So, the quantities q^+ and q_{ie} have larger values and the electrons temperature increases more clearly in the inner regions.
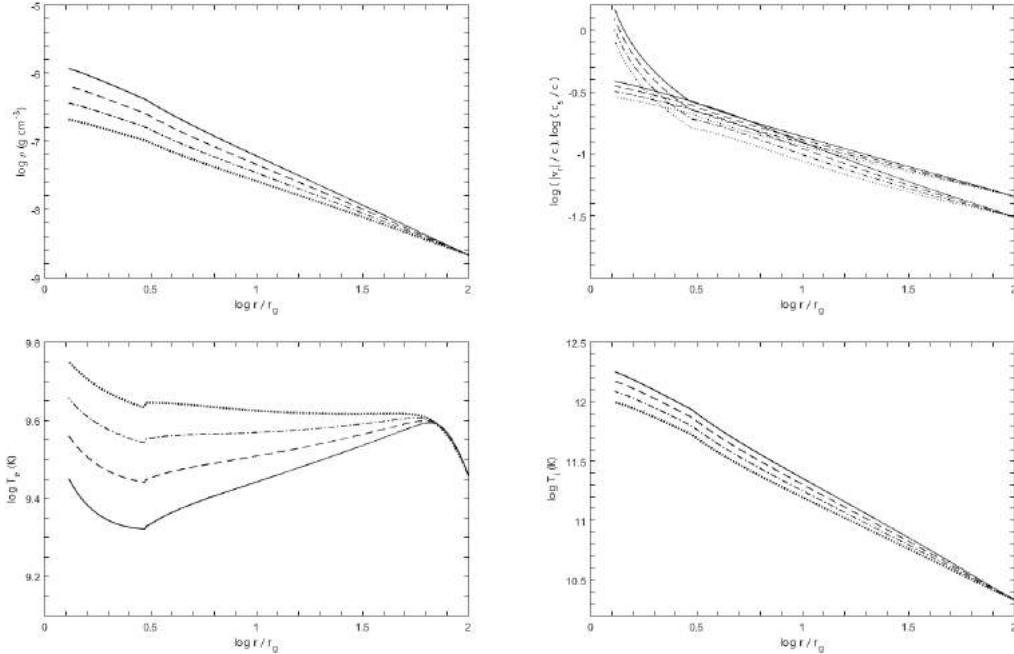

Figure 4: Radial dependency of density, radial velocity, ions temperature and electrons temperature for $s = 0$, $s = 0.2$, $s = 0.4$ and $s = 0.6$ are represented by solid, dashed, dash dotted and dotted lines respectively. The outer boundary radius is$10^2 r_g$ and the boundary conditions are $T_i = 0.6T_{vir}$ and $T_e = 0.08T_{vir}$. $\alpha = 0.3$ and $\dot{M}_{out} = 10^{-1}\dot{M}_{edd}$.

4 Summary

The observational evidence indicates the outflow exists in the accretion flow systems. For this reason, the study of structure of accretion flow in the presence of outflow is important. The spectral models for accretion flows with outflow have been investigated before in the frame of global solution. In these studies, a power law function of radius has been considered for the mass accretion rate and the other dynamical equations of the flow remain unchanged. Also, in these works, the emitted spectra has been taken into account.

In this paper, we focus on the structure of accretion flow in the presence of outflow. To overcome to difficulty of calculation the global solution, we use a simplified global solution to obtain the dynamical structure of accretion flow. We consider an advection dominated accretion flow and use a power law function for mass accretion rate to take into account the role of outflow. In spite of the simplifications that we imposed, our results have a acceptable agreement with the physical predictions.

Although if we want to have a full investigation, the other equations of the flow must be modified and the effects such as the angular momentum and energy transfer should be

considered; as Xie & Yuan (2008) noted, the most important effect of outflow is on the density profile that is caused by the radial variation of mass accretion rate. If the strength of outflow that is determined by s is fixed, all other effects of outflow can only produce a difference for the density and temperature within a factor of ~ 2 [14]. So, we hope the simple method we used does not cause the significant error.

References

[1] Abramowicz, M. A., Chen, X., Kato, S., Lasota, J.-P., & Regev, O. 1995, ApJ, 438, L37

[2] Blandford, E. G., & Begelman, M. C. 1999, MNRAS, 303, L1

[3] Beckert, T. 2000, ApJ, 539, 223

[4] Bu D., Yuan F., & Xie F., 2009, MNRAS, 392, 325

[5] Chen, X., Abramowicz, M. A., Lasota, J.-P., Narayan, R., & Yi, I. 1995, ApJ, 443, L61

[6] Hawley, J. F., & Balbus, S. A. 2002, ApJ, 573, 738

[7] Igumenshchev, I. G., Narayan, R., & Abramowicz, M. A. 2003, ApJ, 592, 1042

[8] Manmoto, T., Mineshige, S., & Kusunose, M. 1997, ApJ, 489, 791

[9] Narayan, R., & Yi, I. 1994, ApJ, 428, L13

[10] Narayan, R., & Yi, I. 1995a, ApJ, 444, 231

[11] Paczyński, B., & Wiita, P. J. 1980, A& A, 88, 23

[12] Quataert, E., & Narayan, R. 1999, ApJ, 520, 298

[13] Stone, J. M., Pringle, J. E., & Begelman, M. C. 1999, MNRAS, 310, 1002

[14] Xie F. G., & Yuan F., 2008, ApJ, 681, 499

[15] Xu, G., & Chen, X. 1997, ApJ, 489, L29

[16] Xue, L., & Wang, J.-C. 2005, ApJ, 623, 372

[17] Yuan, F., Quataert, E., & Narayan, R. 2003, ApJ, 598, 301

[18] Yuan, F., Ma, R.Y., & Narayan, R., 2008, ApJ, 679, 984

[19] Yuan, F., Xie, F., & Ostriker, J. P. 2009, ApJ, 691, 98

Modeling Magnetic Field in Heavy ion Collisions Using Two Different Nuclear Charge Density Distributions

Susan Abbas Nejad[1] · Supervisor: Dr. Umut Gürsoy[2]

1   University College Utrecht, Utrecht, The Netherlands,
    email: susanabbasnejad@gmail.com
2   Department of Physics, Utrecht University, Utrecht, The Netherlands

Abstract. By studying the properties of matter during heavy-ion collisions, a better understanding of the Quark-Gluon plasma is possible. One of the main areas of this study is the calculation of the magnetic field, particularly how the values of conductivity affects this field and how the field strength changes with proper time. In matching the theoretical calculations with results obtained in lab, two different models for charge density distribution inside ions is used. In this study, after explanation of some theoretical background, the magnetic field contribution of the spectators and participants in Pb-Pb ion collision is calculated in a conductive medium and vacuum. Results are compared using two different nuclear charge density models.

Keywords: Quark-Gluon Plasma, QCD, Heavy Ion Collisions, Electromagnetic field, Nuclear density distributions,

1   Introduction

One of the main areas of modern theoretical Physics is the theory of Quantum Chromodynamics (QCD for short). This theory studies the strong force which mainly acts between quarks and gluons. As the name suggests, this plasma is a soup of quarks and gluons. As predicted by this theory, matter at high energy changes into a quark gluon plasma phase. Some theories state that the universe was in this state in the "Quark Epoch", 10^{-12} until 10^{-6} seconds after the big bang [12]. This is also most likely the state of matter at the core of neutron stars [16]. This phase of matter is, thus, very interesting to study.

Since this phase transition is obtained at very high temperatures (thus high energies as well), it can only be obtained on Earth in laboratories like CERN (see figure 1 for a depiction of these experiments). At CERN, this state of matter is obtained by colliding lead ions together at near the speed of light with the nuclei having energies of a few trillion electron-volts each [2]. When two ions are collided together at very high speed, the result will be quark-Gluon plasma (QGP for short) formation for a short period of time (A sketch of the collision is shown in figure 1). Creating this phase of matter at these laboratories helps to study the structure of hadrons at high energy and how the QGP is thermalized. One of the steps in studying this medium is the study of its electromagnetic field. This thesis will focus on the magnetic field in such a collision using two different models describing the nucleon density.

Before describing the theory, it is useful to mention some characteristics of heavy-ion collisions:

1) One of the characteristics of a heavy-ion collision is its centrality. Collisions are mostly not head-on. Figure 1 again shows a sketch of an off-central collision. The center-to-center
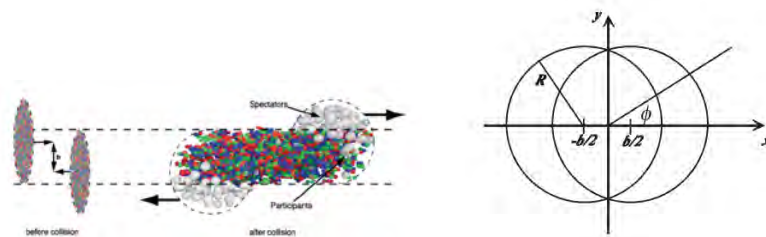
Figure 1: Right: Sketch of an off-central collision. For the spectators one integrates over the two crescent-shaped parts of the two ions and for the participants, one integrates over the almond shaped part in the middle and accounting for both the ion moving in the +z direction and -z direction Left: The set-up of a heavy-ion collision

distance of the two ions is denoted by b. This constant expresses the level of centrality of the collision.

2) As the two ions are travelling at 99.9999 percent the speed of light [4], the ions will be strongly Lorentz contracted (contracted to 1 percent of their original size. See [8]). As a result, in this paper we assume that the neutrons and protons reside on a flat disk as this is an appropriate simplifying approximation.

3) As the collision is not head-on, there are two parts to the collision: the participants (participating in the collision) and the spectators (not participating in the collision) [17]. As seen in figure 1, the participant part of the collision is the area where the two circles meet and the spectators reside on the rest of the area of the two circles (representing ions). In modeling the magnetic field of this plasma, we differentiate between these two parts for reasons which shall be explained. We shall also compare their contribution to the total magnitude of the field. The calculated magnetic field in this thesis will be an interpolated function of proper time. Thus, we will also see how this field changes with time. Before moving on any further, it is helpful to express that we use the Natural Units system in this paper as it is widely used in particle physics. As for the constants used in this thesis, we shall use the constants obtained by measurements taken at the Pb-Pb collision experiments at CERN which started in 2010 [21].

1.0.1   The electromagnetic field of one charge in conductive environment

The environment around a quark gluon plasma has a certain conductivity. As we shall see, this conductivity is such that it is negligible a very short time after the collision but it will affect the magnetic field a very short while afterwards (perhaps as the value of conductivity itself increases).

To find the expression for the Electromagnetic fields in this case, we first take Maxwell's equations with conductivity included. Then, we find the expression for the magnetic field. Knowing the magnetic field at any point in space will also give us the electric field at that point.

Replacing expressions from Maxwell's equations and the expression for Z, we get the equation for the magnetic field:

$$\nabla^2 \vec{B} - \frac{\partial^2 \vec{B}}{\partial t^2} - \sigma \frac{\partial \vec{B}}{\partial t} = -ev\vec{\nabla} \times (\hat{z}\delta_{(z-vt)}\delta_{(x_\perp - x_\perp)})$$

Since the differential operators here are linear, we can use the method of Green's function to solve for B.

And the B field becomes:

$$eB_y = 2^{\alpha_{em}}\hat{y}\int\int\frac{J_1(bk_\perp)k_\perp^2}{\frac{\omega^2}{v^2}+k_\perp^2-\omega^2-i\sigma\omega}e^{i\omega(\frac{z}{v}-t)}dk_\perp d_\omega$$

Here, as the particle is moving at a speed very close to the speed of light, we can make the simplifying assumption that $v = c = 1$. In this case, the magnetic field will be:

$$eB_y = 2\alpha_{em}\hat{y}\int\int\frac{J_1(bk_\perp)k_\perp^2}{k_\perp^2-i\sigma\omega}e^{i\omega(z-t)}dk_\perp d_\omega$$

From here, we proceed first by solving the integral over omega. This integral can be solved using the residue theorem from complex analysis. According to this theorem, the integral of a function over a closed curve is:

$$\int f_{(z)}d_z = 2\pi i\Sigma Res(f,a_k)$$

Where a_k are the poles of the function. Here, there is only one pole at $\frac{k_\perp^2}{i\sigma}=\omega$. So, we get:

$$\int\frac{e^{(i\omega(z-t))}}{i\sigma(\frac{k_\perp^2}{i\sigma}-\omega)}d_\omega = 2\pi i\Sigma Res(f,a_k=\frac{k_\perp^2}{i\sigma})$$

Where the residue is:

$$Res(f,a_k=\frac{k_\perp^2}{i\sigma}) = Lim_{\omega\frac{k_\perp^2}{i\sigma}}\frac{e^{i\omega(z-t)}}{i\sigma} = \frac{1}{i\omega}e^{i\frac{k_\perp^2}{i\sigma}(z-t)}$$

So, the integral becomes:

$$eB_y = \frac{4\pi\alpha_{em}}{\sigma}\hat{y}\int J_1(bk_\perp)e^{\frac{k_\perp^2}{\sigma}(z-t)}k_\perp^2 dk_\perp$$

The integral over $k_\perp$ can be evaluated analytically:

$$eB_y = \hat{y}\frac{\alpha_{em}b\sigma}{2(t-z)^2}e^{\frac{b^2}{e^4(t-z)}}$$

However, for a more accurate calculation, we take $v\neq 1$. Thus, in this case we have:

$$eB_y = \frac{\alpha_{em}}{\pi}\hat{y}\int J_1(bk_\perp)k_\perp{}^2dk_\perp\int\frac{e^{i\omega(\frac{z}{v}-t)}}{\frac{\omega^2}{v^2}+k_\perp^2-\omega^2-i\sigma\omega}d\omega$$

$$eB_y = \frac{\alpha_{em}}{\pi}\hat{y}\int J_1(bk_\perp)k_\perp^2 dk_\perp\int\frac{e^{i\omega(\frac{z}{v}-t)}}{\frac{\omega^2}{v^2}+k_\perp^2-\omega^2-i\sigma\omega}d_\omega$$

In this case, we have two poles:

$$\omega_\pm = \frac{i\sigma\lambda^2v^2}{2}(1\pm\sqrt{1+\frac{4k_\perp^2}{\sigma^2\lambda^2v^2}})$$

Here, we pick only the ω_- part as with the other one, the function for B would diverge. Picking ω_- and calculating the residue for this pole, we get for the field:

$$eB_y = \frac{\alpha_{em}}{\pi}\hat{y}\int \frac{J_1(bk_\perp)k_\perp^2 e^{(-\omega_-(\frac{z}{v}-t))}}{\sigma(1+\frac{4k_\perp^2}{\sigma^2\lambda^2v^2})^{1/2}}dk_\perp$$

To calculate the integral, we first change the variables in the following way:

$$u = (1+\frac{4k_\perp^2}{\sigma^2\lambda^2v^2})^{1/2} \qquad\qquad \frac{du}{dk_\perp} = \frac{1}{u}\frac{4k_\perp}{\sigma^2\lambda^2v^2}$$

$$u^2 - 1 = \frac{4k_\perp^2}{\sigma^2\lambda^2v^2} \qquad k_\perp = \frac{\sigma\lambda v}{2}\sqrt{u^2-1} \qquad dk_\perp = u(\frac{\sigma^2\lambda^2v^2}{4k_\perp})du$$

So, the field becomes:

$$eB_y = \frac{\alpha_{em}}{\pi}\hat{y}\int \frac{2J_1\frac{b\sigma\lambda v}{2}\sqrt{u^2-1}(\frac{\sigma^2\lambda^2v^2}{4})^2\sqrt{u^2-1}}{\sigma^2\lambda v}e^{-\frac{\sigma\lambda^2v^2}{2}(1-u)(t-\frac{z}{v})}du$$

Putting the constant terms to the left side of the integral:

$$eB_y = \frac{\alpha_{em}}{2\pi}[\frac{b\sigma^3\lambda^4v^4}{8}e^{-\frac{\sigma\lambda^2v^2}{2}(t-\frac{z}{v})}]\int J_1(\frac{b\sigma\lambda v}{2}\sqrt{u^2-1})\sqrt{u^2-1}e^{-\frac{\sigma\lambda^2v^2}{2}(t-\frac{z}{v})u}du$$

Now, we have the B field in terms of the normal variables (x,y,z,t) and v. However, there is a more convenient coordinate system to describe heavy ion collisions. That system uses τ (proper time) , η (pseudo-rapidity) , $x_\perp$ (distance from the center of the ion to where we want to find the field) and ϕ (angel from x axes to the line of $x_\perp$).

Pseudo-rapidity in natural units is a dimension-less coordinate which is similar to a hyperbolic angel [21]. In this system of coordinates, instead of using speed, we use a similar constant related to speed called rapidity Y. These variables are the experimental observables in heavy ion collision experiments and thus are more convenient to work with [18]. The transformations from Cartesian coordinates to the new coordinates are as follows:

$$\tau = \sqrt{t^2-z^2} \qquad \eta = arctanh(\frac{z}{t}) \qquad x_\perp = \sqrt{x^2+y^2}$$

$$\varphi = acrtan(y/x) \qquad Y = arctanh(\frac{v_z}{C}) \qquad z' = \beta t$$

And the other way:

$$t = \tau Cosh(\eta) \qquad x = x_\perp Cos(\varphi) \qquad y = x_\perp Sin(\varphi)$$

$$z = \tau sinh(\nu) \qquad v = tanh(Y)$$

At this stage, one should consider taking into account the correct range for the variables. As it can be seen, $\eta = 0$ corresponds to the t-axis and $\eta = \pm\infty$ corresponds to the light cone ($z = t$). As the results do not depend on the pesudo-rapidity window in which we initialize the particles (as long as it is larger than the observed rapidity bins), for most studies, the ammount $-3 < \eta < 3$ is sufficient [3]. This value is also within the window of pseudo-rapidity calculations in ALICE [22]. For rapidity, we also use the value $Y_0 \simeq 7.6$ used in the
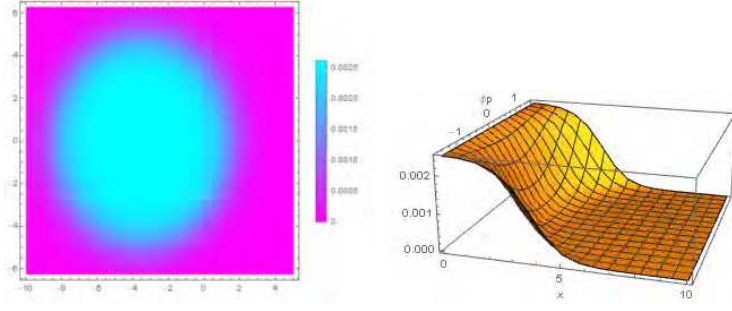
Figure 2: Right: Plot of the number density function (equation 2.1) for Woods-Saxon model in termsof x and y for lead ion the center of which is positioned at $x_{\perp 0} = 3.5$. The Plot-Legendon the right shows the relative value for the number density function for the correspondingcolour. As we can see here, the density is highest at the center and lowest as we go to theborders of the ion as expected.Left: 3D plot of the number density as a function of $x'_\perp$ and ϕ'. It is visible that along a constang angel, as x increases, the number density decreases. This drop in density is similar to the drop in Woods-Saxon potential as a function of x; as expected.

LHC experiments [1]. As for τ, we use the proper time until the time of thermalization. It is known that the proper time of thermalization is about 0.5 fm [23].

This integral can again be calculated analytically:

$$eB_y = \frac{2\pi(\lambda^2\sigma^2\upsilon^2)}{4}\frac{\lambda\upsilon}{2}e^{(t-\frac{z}{\upsilon})\frac{\sigma\lambda^2\upsilon^2}{2}}\sqrt{\frac{2}{\pi}}\beta(\alpha^2+\beta^2)^{-3/4}K_{3/2}(\sqrt{\alpha^2+\beta^2})$$

Where

$$K_{3/2}(z) = \frac{2}{\pi}e^{-z(1+\frac{1}{z})}$$

1.1   Coordinate transformations:

The magnetic field in terms of the new variables is:

$$eB_y^+(\tau,\eta,x_\perp,\phi) = \alpha\sinh(Y_b)(x_\perp\cos\phi - x'_\perp\cos\phi')\frac{(\frac{|\sinh(Y_b)|}{2}\sqrt{\Delta}+1)}{\Delta^{\frac{3}{2}}}e^A,$$

where $\alpha = e^2/(4\pi)$ is the electromagnetic coupling constant, $Y_b \equiv (\beta)$ is the rapidity of the particle moving in the +z direction. We have also defined:

$$A = \frac{\sigma}{2}(\tau\sinh(Y_b)\sinh(Y_b-\eta) - |\sinh(Y_b)|\sqrt{\Delta}$$

$$\Delta = \tau^2\sinh^2(Y_b-\eta) + x_\perp{}^2 + (x'_\perp)^2 - 2\times x_\perp\times x'_\perp\times\cos(\phi-\phi')$$

We only take into account the y component of the field since we will be studying the field evolution at around the center where this component is the main component of the field as also stated by [8]. Knowing the Magnetic field, one can find the Electric field as follows:

$$eE_x^+(\tau,\eta,x_\perp,\phi) = eB_y^+(\tau,\eta,x_\perp,\phi)\coth(Y_b-\eta)\,.1.4$$

So now we have the x,y and z part of the Electric and magnetic field for one moving particle in lab frame (calculations also carried out by [1] , [20]).

2 Numerical Integration

At this stage, we have the contribution to the magnetic field for only one particle. Our aim is to integrate over the contributions of the field from all the particles on the 2D ion discs (see figure 2).

As we will see later, the integral, when found, will be a function of $(\eta, \tau, \phi, x_\perp)$. This integral cannot be found analytically as it is too complicated. Hence, we use numerical integration to find a good approximation to the integral.

In this section, we discuss the assumptions and models used to do this integration. First, two different models for particle distribution functions inside the ions are introduced. Afterwards some theories regarding relations with proper time are discussed. Finally, the magnetic field is calculated using the two models and the results are compared.

2.1 Two Different Nuclear Distribution Function Models

To find the magnetic field of the moving ion, we have to add up the contributions due to all the particles (see figure 1). For this purpose, we use two different models for distribution of protons inside the nuclei. As we shall see, the hard-sphere distribution is more simplified than the Woods-Saxon distribution which may be unrealistic in some situations. Thus, in following the numerical calculation of the magnetic field, we use both these distributions to compare them with previously obtained results.

2.1.1 The Woods-Saxon Model

The more accurate of the two nuclear Distribution Function models is called the Woods-Saxon model where the number density of protons is given by the equation bellow (see also [24] and [1]):

$$n_A(r) = \frac{n_0}{1 + e^{\frac{r-R}{d}}} \quad 2.1$$

Where R is the radius of the nuclei and r is the distance from the center of nuclei. The values for constants are $n_0 = 0.17 fm^{-1}$ and $d = 0.54 fm$ and $R = 7 fm$. The distance from the center of nuclei in terms of the x-y-z coordinates is:

$$r_\pm = \sqrt{\left(x \pm \frac{b}{2}\right)^2 + y^2 + z^2}$$

Switching to the new coordinate system:

$$r_\pm = \sqrt{(x'_\perp \pm bx'_\perp Cos(\phi')) + \frac{b^2}{4} + (z - \tau^2 Sinh^2(\eta))}$$

Figure 3 shows some plots of the number density function (2.1):

To get the density at any $(x_\perp , \phi p)$, we integrate over z (see the integral bellow). The reason for the original z-dependence is due to the uncertainty in the position of each particle along the z direction.

$$\rho_\pm(x'_\perp) = \frac{1}{N} \int dz' \frac{n_0}{1 + e^{\frac{r-R}{d}}} \quad 2.2$$

Where N is the normalization factor. The values for constants are $n0 = 0.17 fm^{-3}$ and $N = 1.6487$ and $d = 0.54 fm$. This integral is also of the type which cannot be evaluated analytically and a numerical calculation must be done to evaluate a near-enough approximation.
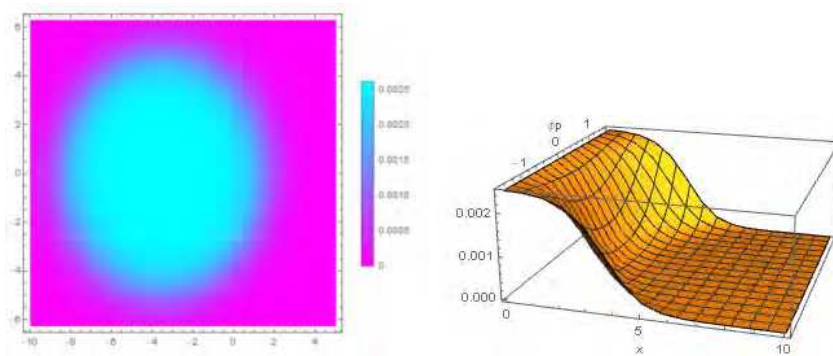
Figure 3: Right: 3D plot of the number density as a function of $x'_\perp$ and ϕ'. It is visible that along a constang angel, as x increases, the number density decreases. This drop in density is similar to the drop in Woods-Saxon potential as a function of x; as expected. Left: Plot of the number density function (equation 2.1) for Woods-Saxon model in terms of x and y for lead ion the center of which is positioned at $x_{\perp 0} = 3.5$. The Plot-Legend on the right shows the relative value for the number density function for the corresponding colour. As we can see here, the density is highest at the center and lowest as we go to the borders of the ion as expected.

2.1.2 Hard-Sphere Model

Another model for the density function of charges within an ion is the Hard-Sphere model which is more simplified and easier to work with:

$$\rho_\pm(x'_\perp) = \frac{3}{2\pi R^3} \sqrt{R^2 - (x'_\perp \pm bx'_\perp Cos(\phi')) + \frac{b^2}{4}} \quad 2.3$$

2.2 A Note on Proper Time

One way to follow the numerical integration is to do so on the freeze-out surface. This surface is a hyper-surface in space-time where hadrons are produced during the collision as the matter cools down which is defined by a function $\tau_{freeze[x_\perp]}$ [21]. Calculation of the magnetic field on this surface decreases the number of variables by one.

Another way, however, is to integrate for the magnetic field at any point in space-time and not just the freeze-out surface. This way requires more computation time but is more accurate.

2.3 Spectator Contribution

At this point, one has to differentiate between the spectators and the participants when doing the numerical integration. For the spectator contribution, the amount of rapidity does not change (the particles are not participating in any reaction and are assumed to move with constant speed before and after the collision), but for the participants, it does change. In our case for Pb-Pb collisions with center-of-mass energy per nucleon pair of about 2 TeV, we take $Y0 \equiv 7.6$ [22]. For the spectator contribution, we only integrate over $x'_\perp$ and ϕ' as follows [1]:

$$\Sigma eB_{s,y} = -Z \int_{-\frac{\pi}{2}}^{\frac{\pi}{2}} d\phi' \int_{x_{in}}^{x_{out}} \rho_\pm(x'_\perp)\theta_\pm(x_\perp)(1 - \theta_\mp(x_\perp))eB_i x_\perp dx'_\perp$$
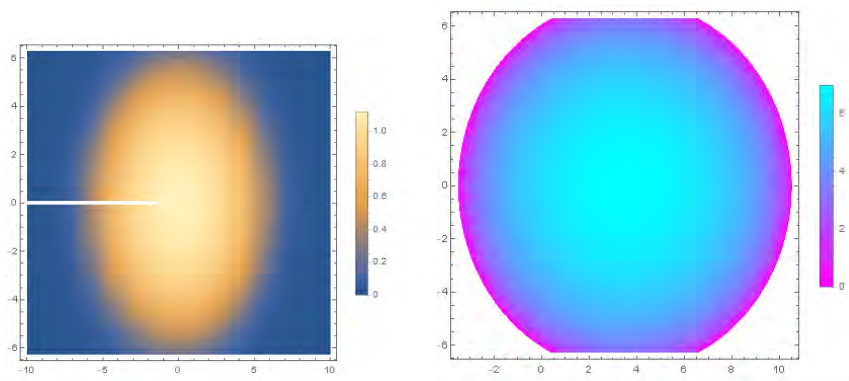
Figure 4: Left: Density plot of the Integrated density function (equation 2.2) for Woods-Saxon model. The integral is approximated by numerical integration (see Appendix) and a function $\rho_{(x_\perp,\phi')}$ is obtained by interpolation. Right: the density-plot of the density function for Hard-Sphere model in terms of x and y for lead ion. The Plot-Legend on the right show the relative value for the density function for the corresponding colour. It is observed that the density is highest at the center and lowest as we go to the borders, exactly as one would expect to get with a sphere of uniformly distributed matter. However, as this model is more simplified, it also looks more symmetric and perfect which may be an unrealistic model in some situations.

Where $\rho_\pm(x'_\perp)$ describes the particle distribution function for a relativistic ion and $\theta_{-(x_\perp)} = \theta[R^2 - (x_\perp - \frac{b}{2}\hat{x})^2]$. We use $Z = 82$ as it is the atomic number for Lead nuclei which is used in heavy ion collisions at CERN. Here, x_{in} and x_{out} describe the crescent shaped loci where we find the particles which are either moving in the +z or -z direction but not both and are described by the following functions [1]:

$$x_{in/out}(\phi') = \mp\frac{b}{2}cos(\phi') + \sqrt{R^2 - \frac{b^2}{4}sin^2(\phi')}$$

The θ functions account for charges moving in the opposite directions. Replacing these functions by the magnetic field as a function of $\phi, \eta, x'_\perp, \tau$ (moving in +z direction) and $\pi - \phi, -\eta, x'_\perp, \tau$ (moving in -z direction) we get:

$$eB_{s,y}^- = -Z \int_{-\frac{\pi}{2}}^{\frac{\pi}{2}} d\phi' \int_{x_{in}}^{x_{out}} x'_\perp \rho_+(x'_\perp)((eB_y^+(\pi - \phi, -\eta, x'_\perp, \tau)) + (eB_y^+(\phi, \eta, x'_\perp, \tau)))dx'_\perp$$

3   Results

3.0.1   Spectator Contribution with The Hard-Sphere Model

For the particle distribution function, we first use the hard-sphere model which is easier to work with. This has been done before by [1] and is done here for comparison. Figure 5 bellow shows the results of the numerical calculation using the density function shown in formula (2.3), with and without conductivity:

It is clear from the figure that the field is very strong at low values of τ . In the short moments before/during/after the impact of two ions in non-central collisions, there is a very strong magnetic field in the reaction zone [5]. In fact, being of order of 10^{18} Gauss, these fields are among the strongest magnetic fields in nature [3].
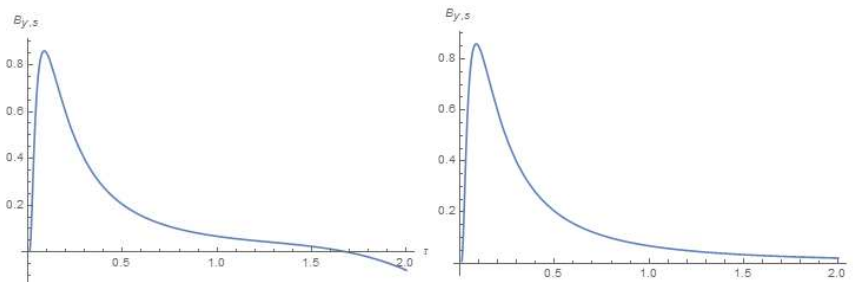
Figure 5: Right: Plot of the interpolated function of B in terms of τ at ($xp = 0.001$, $\phi = \frac{\pi}{2}$, $\eta = 0.1$) with the exception of having non-zero conductivity ($\sigma = 0.023$). Again, results are similar enough to [1]. Left: Plot of the interpolated function of total B field in terms of τ at ($xp = 0.001$, $\phi = \frac{\pi}{2}$, $\eta = 0.1$) in medium with zero conductivity. The maximum value of the field is $0.85 fm^{-2}$ which, upon conversion gives us 1.7×10^{18} Gauss. As expected, results are similar to [1]. The part of the graph that is negative is a result of extrapolation and shall be ignored.

As can also be seen, these fields decay almost immediately (put the values in seconds). However, including the effects of a conducting medium, the field decays slower (see also [5] and figure 6 bellow).

3.0.2   Spectator Contribution with Woods-Saxon Model

To calculate the field using this model, we use the function obtained by interpolation (described in section 2.1.1). Figure 7 bellow shows the obtained result with conductivity. The maximum value here is about $0.95 fm^{-2}$. Compared with the maximum value of about $0.84 fm^{-2}$ it shows a higher but close-enough value.

3.0.3   Participants

Unlike the calculation of the B-field for Spectators where the rapidity Y does not change (because they do not collide with particles from the other direction), for the participant contribution to the field, we have to take into account the change in rapidity. Thus, to get the total field we will also integrate over the distribution of Y given by the equation bellow ([8] and [9]).

$$f(Y_b) = \frac{a}{2 Sinh(aY_0)} e^{aY_b} 2.4$$

Where $-Y_0 < Y_b < Y_0$ [1] and $Y0 \approx 7.6$ and $a \approx 0.5$. Thus the total field will be [1]:

$$eB_{y,p} = -Z \int_{-Y_0}^{Y_0} f(Y_b) dY_b \int_{-\frac{\pi}{2}}^{\frac{\pi}{2}} d\phi' \int_0^{x_{in}(\phi')} \rho_{\pm}(x'_{\perp}) \theta_{\pm}(x_{\perp})(1 - \theta_{\mp}(x_{\perp})) eB_i x_{\perp} dx_{\perp}$$

3.0.4   Participants Contribution With The Hard-Sphere Model

As for the participants contribution to the Magnetic field using the Hard-Sphere model, the maximum of the field is only about $0.065 fm^{-1}$, i.e. about only a hundredth of the contribution of the spectators. This is mainly due to the fact that there are less particles participating in the collision.
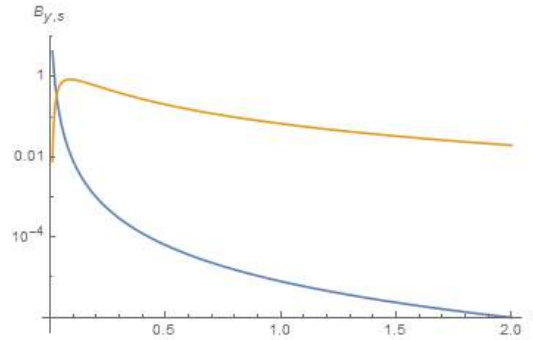
Figure 6: Figures 9 and 10 plotted together. The blue line shows the field without conductivity and the orange line shows the field including conductivity. As can be seen, a conductive medium slows down the decay of the magnetic field. In the very early times, the plot using a medium without conductivity is more accurate as the conducting medium is not formed immediately as quarks take some time to be created from the Glasma field [13]. Also we assumed that the medium does not alter during the evolution of QGP, thus the usage of a constant value for conductivity. However, as also seen from the graph, a decrease in conductivity due to expansion of the medium will only increase the decay speed of the magnetic field [13].
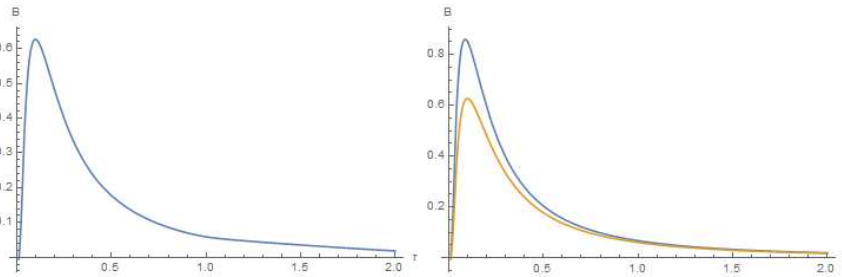

Figure 7: Right: Spectator contribution using Woods-Saxon Model (orange) and Hard-Sphere (blue) plotted together. As seen, both are within the order of magnitude window of 10^{18} Gauss which, in the realm of the strong fields produced as a result of heavy ion collisions, is close enough. Left : Spectator contribution to the magnetic field using Woods-Saxon Model in conductive medium.
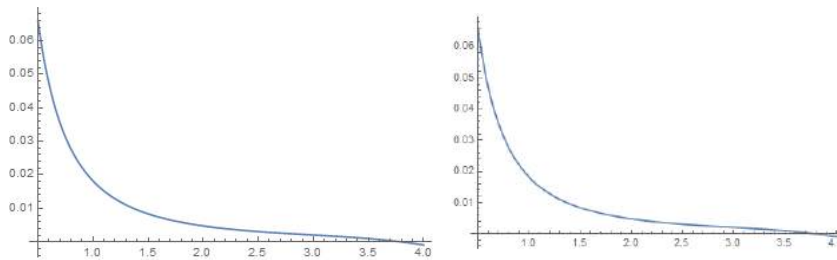

Figure 8: Left: Plot of the proper-time dependence of the magnetic field of the participants using the Woods-Saxon model. right: Plot of the proper-time dependence of the magnetic field of the participants using the Woods-Saxon model.

3.0.5 Participants contribution with Woods-Saxon Model

Figure 8 bellow shows the same contribution using the Woods-Saxon model. Again, the maximum value of the field is the same and about $0.065fm^{-1}$ showing that the two models produce similar results in the case of the participants.

4 Discussion

In heavy-ion collisions, the nuclei pass each other at very high velocity. In these high energy situations, the confined matter inside the ions turns into the unconfined QGP. It is found that the relativistically moving heavy ions, typically with large positive charges, carry strong magnetic (and electric) fields with them. In the short moments before/during/after the impact of two ions in off-central collisions, there is a very strong magnetic field in the reaction zone. In fact, such a magnetic field is estimated to be of the order of 10^{18} Gauss, probably the strongest magnetic field in the present universe [15]. Since the distances between the nucleons are very small (i.e. very close to the reaction time and shortly afterwards), one would expect that the magnetic field of such reactions is very high. As argued by [14], observation of Lepton polarization can prove the existence of such strong fields in heavy-ion collision experiments.

In this study, we employed a semi-analytical model taking relativistic heavy ions as two Lorentz-contracted spheres of charge densities described by two different models. Ignoring interactions of particles we have then compared the resulting magnetic field obtained as a function of proper time. In our results we obtained the spectator contribution to the field which at its maximum has the strength of about 1.7×10^{18} Gauss using the Hard-Sphere model and 1.2×10^{18} Gauss for the Woods-Saxon model. We have also shown that the contribution to the field from the participants is negligible and that taking into account the conductivity, the field decays much slower.

Finally, we have argued that our results using the Woods-Saxon model match; in order of magnitude and up to statistical fluctuations, to results obtained using the approximation of a homogeneously-charged sphere by [1] , [13]. Therefore, we conclude that due to its simplicity, the Hard-Sphere model for charge distribution is a good-enough approximation when calculating electromagnetic fields in heavy ion collisions.

5 Potential topics for Further research

As we have seen, an enormous magnetic field can indeed be created in off-central heavy-ion collisions. At this point, a topic for further research could be:

We have seen that the magnitude of the created magnetic field drops as a function of proper time. This change in the magnetic field induces an electric field circulating around the direction of B_y by Faraday's Law. This electric field in turn creates a current which again induces an electric field in the z direction by the Lenz rule. Study of the effects of these inductions on the evolution of the colliding system is an interesting topic for further research (see also [14]).

Acknowledgment

References

[1] Gursoy, Umut and Kharzeev, Dmitri and Rajagopal, Krishna, 2014, Physical Review C, 89, 5

[2] Müller, Berndt and Schukraft, Jürgen and Wysłouch, Bolesław, 2012, Annual Review of Nuclear and Particle Science, 62, 361-386

[3] Greif, Moritz and Greiner, Carsten and Xu, Zhe, 2017, archive , arXiv:1704.06505,

[4] Boissé http://cerncourier.com/cws/article/cern/53089

[5] Zhong, Yang and Yang, Chun-Bin and Cai, Xu and Feng, Sheng-Qin, 2014, Advances in High Energy Physics

[6] Wong, Cheuk-Yin, 1994,World scientific

[7] Marcus, Eric, 2015

[8] Kharzeev, Dmitri E and McLerran, Larry D and Warringa, Harmen J, 2008, Nuclear Physics A, 803, 3-4, 227-253

[9] Kharzeev, D, 1996,Physics Letters B, 378, 1-4

[10] Schukraft, Jurgen and Stock, Reinhard, 2015, arXiv preprint arXiv:1505.06853

[11] Widrow, Lawrence M and Ryu, Dongsu and Schleicher, Dominik RG and Subramanian, Kandaswamy and Tsagas, Christos G and Treumann, Rudolf A, 2012, Space Science Reviews, 166, 1

[12] Allday, J, 2002

[13] McLerran, L and Skokov, V, 2014, Nuclear Physics A, 929, 184-190

[14] Tuchin, Kirill, 2010, Physical Review C, 82, 3

[15] Grasso, Dario and Rubinstein, Hector R, 2001, Physics Reports, 384, 3

[16] Duncan, Robert C and Thompson, Christopher, 1992, The Astrophysical Journal, 392, L9–L13

[17] URL: http://cerncourier.com/cws/article/cern/53089

[18] Foka, Panagiota and Janik, Małgorzata Anna, 2016, Reviews in Physics, 1, 154–171

[19] Bjorken, James D, 1983, Physical review D, 27, 1, 140

[20] Deng, W.T. and Huang, X.G., 2012, Physical Review C, 85(4), p.044907.

[21] Tarafdar, S. and Singh, V.

[22] ALICE collaboration and others, 2014, Physics Letters B, 734, 314–327,

[23] Patra, BK and Alam, Jan-e and Roy, Pradip and Sarkar, Sourav and Sinha, Bikash. and Singh,2002, Nuclear Physics A, 709

[24] De Jager, CW and De Vries, H and De Vries, C, 1974, Atomic data and nuclear data tables, 14, 5-6

Soliton-like Solutions of the Complex Non-linear Klein-Gordon Systems in $1 + 1$ Dimensions

Mohammad Mohammadi[1] · Ali Reza Olamaei[2]

[1] Physics Department, Persian Gulf University, Bushehr 75169, Iran.;
    email: physmohammadi@pgu.ac.ir
[2] Physics Department, Jahrom University, Jahrom 74135-111, Iran;
    email: olamaei@jahromu.ac.ir

Abstract. In this paper, we present soliton-like solutions of the non-linear complex Klein-Gordon systems in 1+1 dimensions. We will use polar representation to introduce three different soliton-like solutions including, complex kinks (anti-kinks), radiative-profiles, and localized wave-packets. Complex kinks (anti-kinks) are topological objects with zero electrical charges. Radiative profiles are objects that move at the speed of light and therefore, have a zero rest mass. They can be created in kink-anti-kink collisions and vice versa. Localized wave packet solutions are non-topological objects for which wave and particle behavior are reconciled in a classical way. For localized wave packet solutions, the trivial initial phase imposes an uncertainty on the collision fates.

Keywords: complex, non-linear, Klein-Gordon, soliton, uncertainty, kink, radiative-profile, wave-packet.

1   Introduction

Nonlinear real Klein-Gordon (KG) systems in $1 + 1$ dimensions with topological kink (anti-kink) solutions have been suited for decades. The most well-known system in this area is the integrable sine-Gordon (SG) system [1, 2, 3, 4]. There are many other systems with kink solutions but are not as famous as the SG system [1, 5, 6, 7, 8, 9, 10, 11, 12, 13, 14]. In spite of wide studies in the real non-linear Klein-Gordon systems with soliton-like kink (anti-kink) solutions, the complex versions were to some extent out of interest [15, 16, 17, 18, 19, 20, 21, 22, 23, 24]. An attempt in this line was the introduction of the complex kink (anti-kink) and radiative profiles, specially for the complex SG system [24].

In general, complex KG systems (Lagrangian densities) are ones which composed of complex fields. In other words, they are just special versions of the KG systems which are functional of scalar fields (ϕ) and their complex conjugates (ϕ^*). For complex KG systems, it is easy to show that the conservation of electrical charge is satisfied generally. In fact, it essentially originates from the $U(1)$ symmetry of such systems. For a real KG system with real scalar fields φ and standard kinetic terms $\partial_\mu \varphi \partial^\mu \varphi$, one can easily change it to a complex version via the following transformations: $\varphi \longrightarrow |\phi| = R = \sqrt{\phi \phi^*}$ and $\partial_\mu \varphi \partial^\mu \varphi \longrightarrow \partial_\mu \phi \partial^\mu \phi^*$.

In this paper, with a straightforward mathematical calculation, all soliton-like solutions of the complex non-linear Klein-Gordon systems (CNKG) in 1+1 dimensions will be studied generally. Complex kinks (anti-kinks), radiative profiles and localized wave-packets are three types of soliton-like solutions which will be considered in details for all CNKG systems. For such systems, two kinds of conserved charge, topological and electrical, can be defined. All complex kink (anti-kink) solutions have the same rest mass and zero electrical charge

but non-zero topological charge. Radiative profiles, as is obvious from their name, travel with the speed of light and have zero rest mass. Regarding radiative profiles, there is a countless variety. They can be topological or non-topological, have zero electric charge or non-zero one. Radiative profiles are created in collision between kinks and anti-kinks, and this process could be happening in the opposite direction; that means in the collision between two radiative profiles, kink-anti-kink pairs can be created.

Localized wave packet solutions, unlike the ordinary (linear) KG equations, do not disperse and they do satisfy a relation similar to the de Broglies wavelength-momentum relation. Two apparently contradictory aspects of quantum behavior, i.e. wave and particle behavior, are reconciled in a classical way for such soliton-like solutions. There are a continuous range of localized wave packet solutions which can be identified by different rest frequencies ω_o. Some of them are not stable and they decompose into a pair of separate kink and anti-kink. It will be shown that there is an uncertainty in the collision processes which is related to trivial initial phases. For different initial phases, particle aspect of the localized wave packets solutions remains unchanged, while the final behaviour in collision processes may be drastically affected. All soliton-like solutions were shown to obey the famous energy-rest mass-momentum relation of the special relativity.

We expect all CNKG systems to have similar features. Therefore, the complex ϕ^4 system as a special example of the CNKG systems in 1+1 dimensions will be employed. Fortunately, we will find well-known analytical functions for its complex kink (anti-kink) and localized wave-packet solutions. All numerical results in this paper will be prepared just for the complex ϕ^4 system. In fact, this paper is the complementary of the pervious paper [24] which was specially about radiative profiles and complex kinks (anti-kinks) of the complex SG system.

The organization of this paper is as follows: In the next section, we will introduce basic equations for non-linear complex KG systems in two different but equivalent representations. Sections 3, 4 and 5 contain a full discussion about complex kinks (anti-kink), radiative profiles and localized wave-packet solutions respectively. Section 6, contains a numerical study about complex kink-anti-kink collisions. In section 7, a numerical study will be prepare for the stability and uncertainty in collisions for the wave packet solutions. The last section devoted to the summary and conclusions.

2   Basic equations

In this paper, we use two different representations to introduce complex non-linear KG systems and related details in $1 + 1$ dimensions. Each of them can shed light on different aspect of the systems, but they are equivalent.

2.1   formal representation

Based on what is done in Refs. [1, 15, 16, 17, 18, 19, 20, 21, 22, 23], the non-linear complex Klein-Gordon systems can be generally introduced by the Lagrangian density as

$$\mathcal{L} = \partial_\mu \phi^* \partial^\mu \phi - V(|\phi|), \tag{1}$$

where ϕ is a complex scalar field and $V(R)$ represents a self-interacting potential that depends only on the magnitude or module of ϕ ($R = |\phi|$). Using the least action principle, the dynamical equation for the evolution of ϕ can be obtained as follows:

$$\Box \phi = \frac{1}{c^2} \frac{\partial^2 \phi}{\partial t^2} - \frac{\partial^2 \phi}{\partial x^2} = -\frac{\partial V}{\partial \phi^*} = -\frac{1}{2} V'(|\phi|) \frac{\phi}{|\phi|}. \tag{2}$$

The energy-momentum tensor corresponding to the Lagrangian density (1) can be calculated using the Noethers theorem:

$$T^{\mu\nu} = 2\partial^\mu \phi^* 2\partial^\nu \phi - g^{\mu\nu}\mathcal{L}, \tag{3}$$

where $g^{\mu\nu}$ is the Minkowski metric tensor. Also, the related energy density has the following form:

$$T^{00} = \varepsilon(x,t) = \frac{1}{c^2}\dot\phi\dot\phi^* + \acute\phi\acute\phi^* + V(|\phi|) \tag{4}$$

where the primes and dots denote space and time derivatives respectively.

Simply, it can be shown that the conservation relation is valid for two four-vector currents; the electrical current

$$j^\mu = i\eta(\phi^*\partial^\mu\phi - \phi\partial^\mu\phi^*), \tag{5}$$

and topological current

$$J^\mu = C\epsilon^{\mu\nu}\partial_\nu\phi. \tag{6}$$

Here $\epsilon^{\mu\nu}$ is an anti-symmetric tensor, C and η are just constant numbers. Corresponding to each of these currents, it can be easily shown that

$$q = \int_{-\infty}^{+\infty} j^0 dx = \int_{-\infty}^{+\infty} i\eta(\phi^*\dot\phi - \phi\dot\phi^*)dx, \tag{7}$$

and

$$Q = \int_{-\infty}^{+\infty} J^0 dx = C[\phi(+\infty) - \phi(-\infty)], \tag{8}$$

that we call them electrical and topological charges respectively, which are constants of motion.

2.2   polar representation

Following the line of Refs. [1, 15, 16, 17, 18, 19, 20, 21], we can change variables ϕ and ϕ^* to polar fields $R(x,t)$ and $\theta(x,t)$ as defined by

$$\phi(x,t) = R(x,t)\exp[i\theta(x,t)]. \tag{9}$$

In terms of polar fields, the Lagrangian-density and field equations transform respectively to

$$\mathcal{L} = (\partial^\mu R\partial_\mu R) + R^2(\partial^\mu\theta\partial_\mu\theta) - V(R), \tag{10}$$

and

$$\Box R - R(\partial^\mu\theta\partial_\mu\theta) = -\frac{1}{2}\frac{dV}{dR}, \tag{11}$$

$$\partial_\mu(R^2\partial^\mu\theta) = 2R(\partial_\mu R\partial^\mu\theta) + R^2(\partial^\mu\partial_\mu\theta) = 0. \tag{12}$$

The related Hamiltonian (energy) density is obtained via the Noether's theorem:

$$\varepsilon(x,t) = \frac{1}{c^2}\dot R^2 + \acute R^2 + R^2(\frac{1}{c^2}\dot\theta^2 + \acute\theta^2) + V(R). \tag{13}$$

The corresponding electrical current is

$$j^\mu = -2\eta(R^2\partial^\mu\theta), \tag{14}$$

which according to field equation (12) is the conserved current.

3 Complex Kink (Anti-kink) solutions

If the phase function $\theta(x,t)$ is a constant, then equation (12) will be satisfied automatically and equation (11) is reduced to

$$\Box R = -\frac{1}{2}\frac{dV}{dR},\tag{15}$$

which is the same as real non-linear Klein-Gordon equation with well-known kink and anti-kink solutions. If $R = \varphi_o(x)$ is the static kink (anti-kink) solution of the equation (15), then a moving complex kink (anti-kink) solution with velocity v would be introduced in the following form:

$$\phi(x,t) = \varphi_v(x,t)e^{i\theta} = \varphi_o(\pm\gamma(x - vt - x_o))e^{i\theta}.\tag{16}$$

in which $\gamma = 1/\sqrt{1 - \frac{v^2}{c^2}}$, and x_o is the initial position of the center of the kink (anti-kink). Generally, to have kink and anti-kink solutions, field potential $V(R)$ must have at least two successive non-negative vacuum points. For complex kinks and anti-kinks solutions (16), in general, it can be shown that the electrical charge (7) is always zero and the topological charge (8) will take the following final form:

$$Q = Ce^{i\theta}[\varphi_v(+\infty) - \varphi_v(-\infty)],\tag{17}$$

Moreover, using the energy-momentum tensor (3), it can be shown simply that in general, these solutions satisfy the relativistic energy-momentum relations as we expect for a real particle:

$$E_v = \gamma E_o = \int_{-\infty}^{+\infty}[\frac{1}{c^2}\dot{R}^2 + \acute{R}^2 + V(R)]dx,\tag{18}$$

$$p = \int_{-\infty}^{+\infty} T^{01}dx = \int_{-\infty}^{+\infty}[\frac{1}{c^2}\dot{\phi}\acute{\phi}]dx = \gamma m_o v,\tag{19}$$

where $E_o = m_o c^2$ is the rest energy of kinks (anti-kinks).

A real KG system with kink (anti-kink) solutions is the famous φ^4 system which is identified by the following Lagrangian density:

$$\mathcal{L} = \partial_\mu\varphi\partial^\mu\varphi - (\varphi^2 - 1)^2.\tag{20}$$

Its standard kink (anti-kink) solution is

$$\varphi(x,t) = \tanh(\pm\gamma(x - vt - x_o)),\tag{21}$$

which varies between -1 and 1 (i.e. the successive vacuum points which are zeros of the potential $U(\varphi) = (\varphi^2 - 1)^2$). There are many works which studied the collisions and internal structures of the real φ^4 system [1, 5, 6, 7, 8, 9]. In this paper, we use this famous real KG system (20) to build the complex version of that. Therefore, the complex ϕ^4 system, as an example of the CNKG systems, can be introduced as follows:

$$\mathcal{L} = \partial_\mu\phi\partial^\mu\phi^* - [(R - 1)^2 - 1]^2.\tag{22}$$

Note that, the module function R must be always positive. Therefore, according to Eq. (15), to have a kink (anti-kink) solution, since a kink (anti-kink) solution varies from one vacuum point to another one, we must use a modified version of the potential (instead of $U(R) = (R^2 - 1)^2$) in such a way that $R = 0, 2 \geq 0$ being vacuum points, i.e.

$$V(R) = [(R - 1)^2 - 1]^2.\tag{23}$$

For this complex field system (22), the corresponding complex kink and anti-kink solutions are

$$\phi(x,t) = [\tanh(\pm\gamma(x - vt - x_o)) + 1]\, e^{i\theta}. \tag{24}$$

The related topological charge, if we choose $C = 1$, is

$$Q = \pm 2e^{i\theta}, \tag{25}$$

in which $+\ (-)$ is for kinks (anti-kinks). In the next sections, specially as an example of the CNKG systems, we use the complex ϕ^4 system to introduce the other soliton-like solutions and study the fates of them in different collisions.

4   Radiative-profile solutions

If R_j is a vacuum point, i.e. $V(R_j) = 0$ and $\frac{dV}{dR}(R_j) = 0$, it is easy to see that equations (11) and (12) are satisfied for infinite soliton-like solutions which move at speed of light:

$$R(x,t) = R_j, \quad \theta(x,t) = f(x \pm ct), \tag{26}$$

where f is an arbitrary function. The related energy density (13) is now reduced to

$$\varepsilon(x,t) = 2R_j^2 \left(\frac{df}{d\widetilde{x}}\right)^2, \tag{27}$$

in which $\widetilde{x} = x \pm ct$. If for an arbitrary function $f(\widetilde{x})$, the corresponding energy density $\varepsilon(x,t)$ is localized, we have a "radiative-profile", i.e. a packet of energy which moves at the speed of light. Moreover, it can be proved generally that for such solutions (similar to massless particles), the relation between total energy and momentum is given by

$$p = \frac{\pm 1}{c} \int_{-\infty}^{+\infty} 2R_i^2 \left(\frac{df}{d\widetilde{x}}\right)^2 = \pm\frac{E}{c}, \tag{28}$$

Equivalently, we can use formal representation to introduce radiative profiles:

$$\phi(x,t) = R_j e^{if(x\pm ct)} = \phi_r(x \pm ct) + i\phi_i(x \pm ct), \tag{29}$$

provided

$$R_j = \sqrt{\phi_r^2 + \phi_i^2}. \tag{30}$$

Namely, for ϕ^4 system (23), to have a radiative profile, if we consider the form of the real part of the field as

$$\phi_r(x,t) = Ae^{-(x\pm ct)^2}, \tag{31}$$

we should consider the imaginary part as the following form:

$$\phi_i(x,t) = \sqrt{4 - A^2 e^{-2(x\pm ct)^2}}, \tag{32}$$

provided that $|A| < 2$. It can be simply conclude that this arbitrary constructed solution (relations (31) and (32)) is a non-topological object with zero topological charge. In general, for any arbitrary solution, depending on functions ϕ_i and ϕ_r to be non-topological (topological) objects, the related topological charge is zero (non-zero). Moreover, for radiative profiles, depending on functions ϕ_r and ϕ_i to be even or odd, the related electrical charges would be zero.

5   wave-packet solutions

It is easy to check that some solutions in the following form:

$$R(x,t) = R(\gamma(x - vt)), \qquad \theta(x,t) = k_\mu x^\mu + \theta_o = \omega t - kx + \theta_o, \tag{33}$$

satisfy equations (11) and (12), provided

$$k = \frac{\omega v}{c^2}, \tag{34}$$

and θ_o (initial phase) is just a constant. In general, $k^\mu \equiv (\omega, k)$ is defined as a $1 + 1$ vector, then $\partial^\mu \theta \partial_\mu \theta = k_\mu k^\mu = \omega_o^2/c^2$ is a constant scalar. Related to different values of ω_o, there are different wave equations for R (11):

$$\Box R = -\frac{d^2 \phi}{d\overline{x}^2} = -\frac{1}{2}\frac{dV}{dR} + \frac{\omega_o^2}{c^2}R, \tag{35}$$

where

$$\overline{x} = \gamma(x - vt). \tag{36}$$

If we multiply (35) by $\frac{dR}{d\overline{x}}$ and integrate, it yields to

$$\left(\frac{dR(\overline{x})}{d\overline{x}}\right)^2 + \frac{\omega_o^2}{c^2}R^2 = V(R) + C', \tag{37}$$

where C' is an integration constant. This constant is expected to vanish for a localized wave-packet. This equation can be easily solved for R, once the potential $V(R)$ is known:

$$\overline{x} - x_o = \pm \int_{R_o}^{R} \frac{dR}{\sqrt{V(R) - \frac{\omega_o^2}{c^2}R^2}}. \tag{38}$$

In general, related to different values of ω_o, there are different non-topological solutions for $R(\overline{x})$. Exactly like complex kink energy-momentum relations (18) and (19), there are the same relations for wave-packet solutions:

$$E_v = \gamma E_o = \gamma \int_{-\infty}^{+\infty}[\acute{R}^2 + R^2 \frac{\omega_o^2}{c^2} + V(R)]dx, \tag{39}$$

$$p = \frac{1}{c^2}\int_{-\infty}^{+\infty}[\dot{\phi}^* \acute{\phi} + \dot{\phi}\acute{\phi}^*]dx = \gamma m_o v, \tag{40}$$

where $E_o = m_o c^2$ is the rest energy of the wave-packet solution and is a function of ω_o. Moreover, one can use equation (34) to obtain

$$\omega = \gamma \omega_o. \tag{41}$$

Therefore, equations (39) and (41) show that frequency and energy have the same behavior and we can relate them via introducing a Planck-like constant $\overline{h}$:

$$E = \overline{h}\omega. \tag{42}$$

It is easy to understand that $\overline{h}$ is a function of rest frequency ω_o and for different wave-packet solutions, there are different $\overline{h}$ constants. Similarity, it is possible to find a relation between relativistic momentum of a soliton solution and wave number k:

$$p = \overline{h}k. \tag{43}$$

This equation is very interesting since it resembles the deBroglie's relation. Note that all Eqs. (34)-(43) were introduced similarly in Ref [22].

If we consider ϕ^4 system (23), the integral (38) can be easily performed, yielding the following solutions for $0 < w_o < 4$:

$$R(\bar{x}) = \frac{(4 - \omega_o^2/c^2)}{2 + \omega_o \cosh(\sqrt{4 - \omega_o^2/c^2}\ \bar{x})}. \tag{44}$$

Accordingly, there are infinite localized soliton-like wave-packet solutions which can be identified with different rest frequencies (ω_o). There are the similar works about the localized wave-packet solutions in the Refs. [22, 23].

6   Kink-anti-kink collisions in complex ϕ^4 system

In general, by preparing the suitable initial condition, we can study kink-anti-kink collisions numerically. For example, when an in-phase kink-anti-kink pair collides, i.e. $\theta_1 = \theta_2$, it treats exactly like what happened for the known real ϕ^4 system. An out-of-phase kink-anti-kink pair, i.e. $\theta_1 \neq \theta_2$, leads to the formation of a pair of radiative profiles in a desired stable localized form after collision (see Figs. 1). If in a kink-anti-kink collision, the phase difference $(\theta_2 - \theta_1)$ is equal to $\frac{\pi}{2}$, they always annihilate each other into two radiative profiles (Fig. 2).
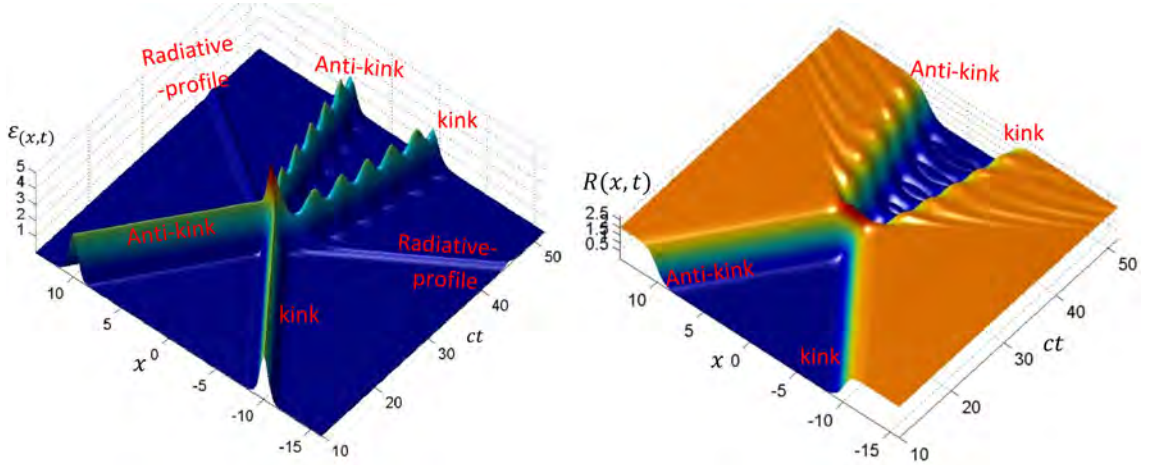
Figure 1: A complex kink ($\theta_1 = \arctan(\sqrt{2})$) collides with a complex anti-kink ($\theta_2 = \frac{\pi}{2}$) with initial kink (anti-kink) speed equals to $0.5c$. For a kink, contrary to an anti-kink, module function change from zero to 2. For radiative profiles, R is always constant ($R = 2$), hence it is not possible to track a radiative profile via the module representation.

Thus, we guess that the reversed process in collision between two radiative profiles would be possible. In other words, we expect we would be able to prepare a condition to create some kink-anti-kink pairs from the collisions of two radiative profiles. Theoretically, the discussion about this matter appears to be very difficult, but with the help of numerical simulations, we can see that in the case of the collision of two energetic radiative profiles, the creation of kink-anti-kink pairs with non-zero rest mass is possible. Although radiative profiles look like ordinary solutions of a linear wave equation, the inherent non-linearity in the original
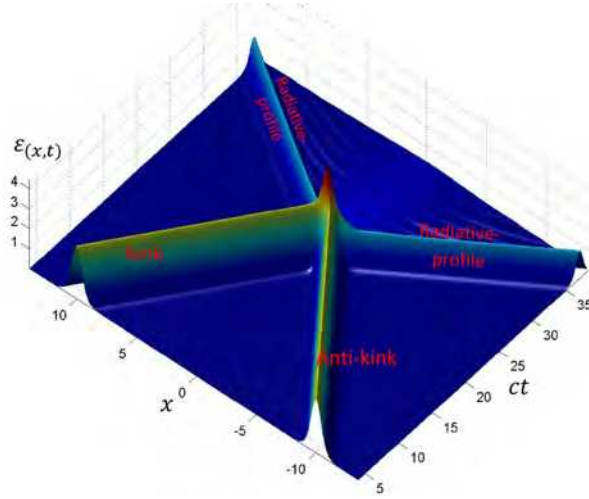
Figure 2: A complex kink (θ_1) collides with a complex anti-kink ($\theta_2 = \theta_1 + \frac{\pi}{2}$) with initial kink (anti-kink) speed of $0.5c$.
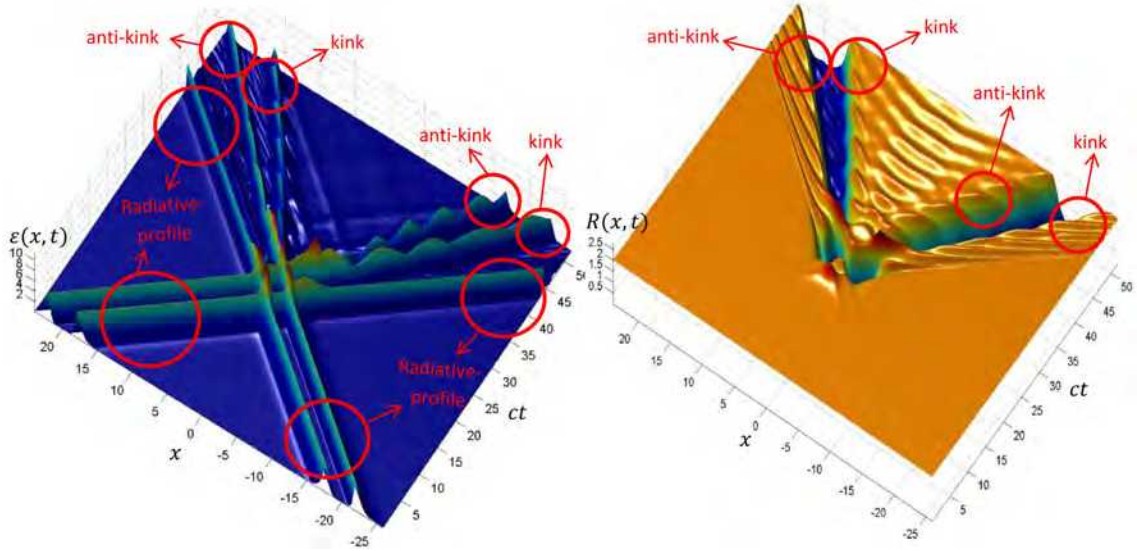

Figure 3: When two radiative profiles collide with each other, pairs of kink-anti-kinks can be created after collision.

field equation causes major differences. Namely, if a pair of similar radiative-profiles which are introduced by

$$\phi_r(x \pm ct) = \frac{2(x \pm ct)^6}{100 + (x \pm ct)^6}, \quad \phi_i = \sqrt{4 - \phi_r^2}, \tag{45}$$

collide with each other, two pairs of kink-anti-kink are created after collision (Fig. 3). It is completely evident that in all of these collisions electrical and topological charges are conserved. There are similar numerical results in the reference [24] which were obtained for the complex SG system.

7 The stability consideration and uncertainty in collisions for the localized wave packet solutions

As we said before, the total rest energy E_o for different localized wave packet solutions is a function of ω_o. For complex ϕ^4 system, the related curve of total rest energy versus ω_o^2/c^2 is shown in Fig. 4. The maximum of this curve occurs almost about $\omega_o^2/c^2 = 0.34$. Numerically, it was shown that for solutions which $\omega_o^2/c^2 < 0.34$, the wave packet solutions are completely unstable i.e. any small perturbation would change it to a pair of separate kink and anti-kink solutions (see Fig. 5). Moreover, for wave packet solutions which ω_o^2/c^2 is more close to 4, the more stability observed numerically.
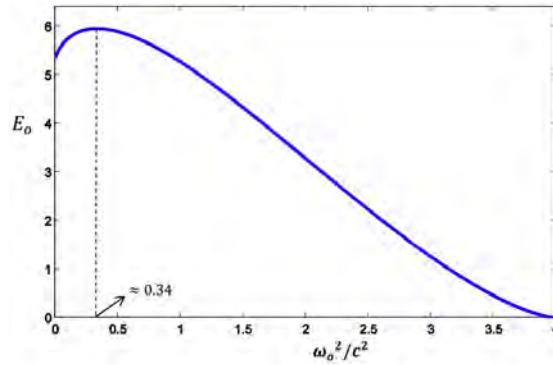
Figure 4: The total rest energy E_o versus ω_o^2/c^2 for different localized wave packet solutions of the complex ϕ^4 system.
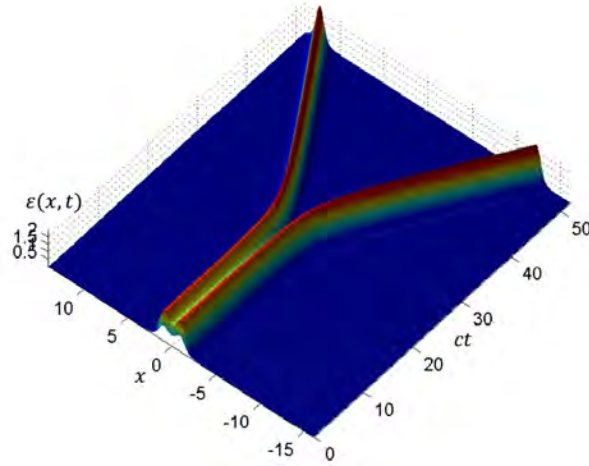
Figure 5: For a localized wave packet solution with $\omega_o^2/c^2 = 0.34$, any small perturbation changes it to a pair of separate kink and anti-kink.

One might think that optional initial phase θ_o for a localized wave packet solution is an unimportant parameter (33). In fact, it has no role in determining basic physical features of a single soliton such as energy, momentum and charge. But, it was seen numerically during the collision between localized wave packet solutions, these initial phases become

very important. Namely, for two identical localized wave packet solutions with $\omega_o^2/c^2 = 0.7$ and initial speed $v = 0.5c$, if the initial phase difference is equal to π i.e. $\theta_{20} - \theta_{10} = \pi$, they are scattered from each other and reappear after collision. But if the initial phase difference is equal to 0, two pairs of kink-anti-kink would appear after collision (Fig. 6). Therefore, there is an apparent uncertainty in the collision processes which originates from the initial phases.
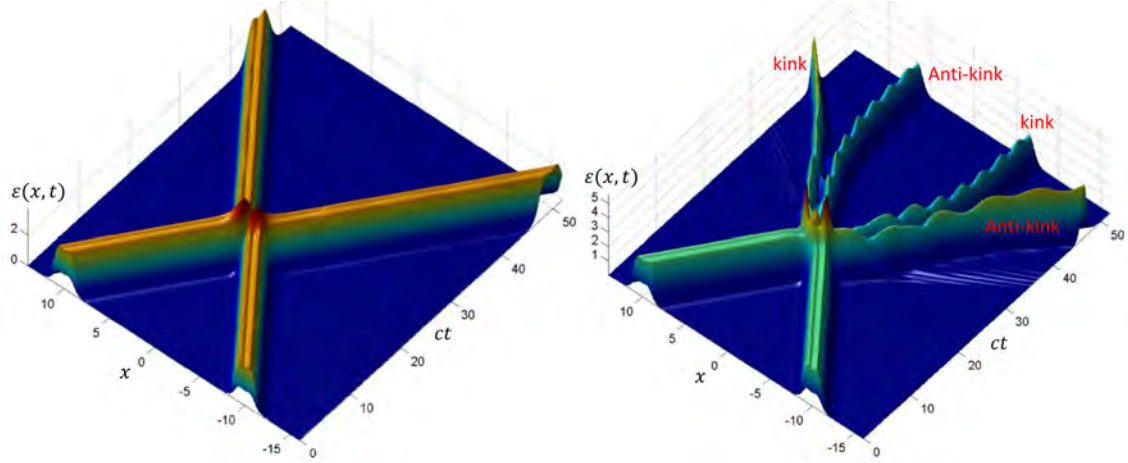

Figure 6: Two identical localized wave packet solutions with $\omega_o^2/c^2 = 0.7$ collide with each other. The initial speeds are $0.5c$. For the left (right) figure, the initial phase difference is π (0).
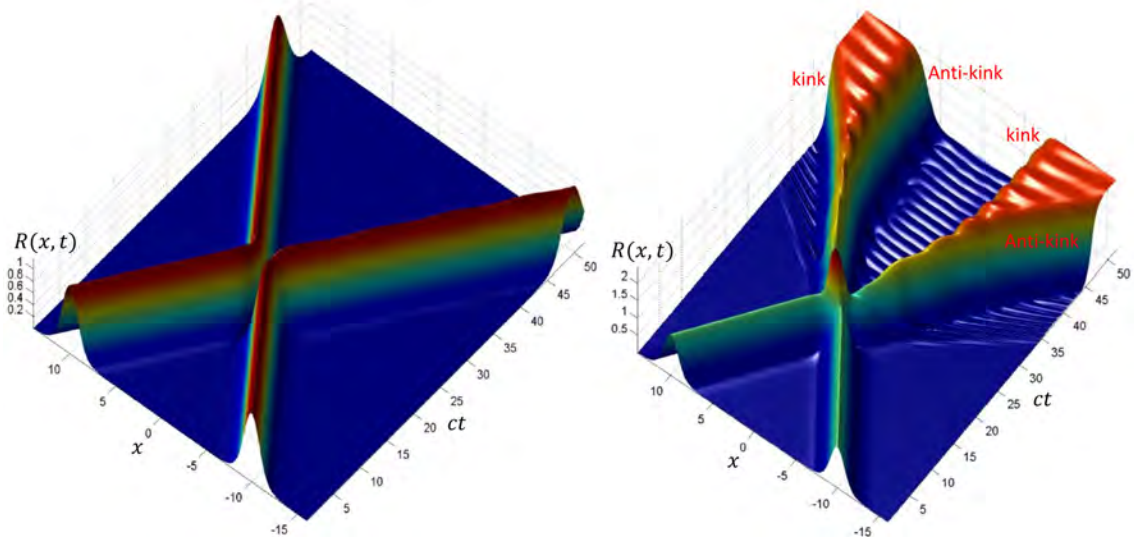
Figure 7: The module representation of Fig. 6. For a kink module function change from zero to 2 contrary to an anti-kink

8 Summery and conclusion

After reviewing some basic properties of the complex non-linear Klein-Gordon (CNKG) equations in two equivalent formal and polar representations, it was shown in general that for the CNKG equations in 1+1 dimensions, there are three different soliton-like solutions: complex kinks (anti-kinks), radiative profiles and localized wave-packets. Complex kinks (anti-kinks) are topological soliton-like solutions with zero electrical charge and the same rest mass. Radiative profiles are localized objects with zero rest mass and move at the speed of light. They can be topological or not, and the related charge may be zero or not. Localized wave-packet solutions are a Continuous range of the soliton-like solutions which can be identified by different rest frequencies (ω_o). Two apparently contradictory aspects of quantum behavior, i.e. wave and particle behavior, were reconciled in a classical way for such soliton-like solutions. All soliton-like solutions were shown to obey the famous energy-rest mass-momentum relation of the special relativity.

In the whole paper, complex ϕ^4 system as a special example of the non-linear complex KG systems in 1+1 dimensions was employed for better consideration of all of the soliton-like solutions. Kink-anti-kink collisions for the complex ϕ^4 system are studied numerically. It was seen that radiative-profiles always appear in out-of-phase kink-anti-kink collisions. In the reversed way, kink-anti-kink pairs can be created in collisions between radiative profiles. It was seen numerically that some of the localized wave packet solutions are completely unstable and decompose into a pair of separate kink-anti-kink solution. Moreover, we found numerically that there is an uncertainty in collision fates between localized wave packet solutions. This uncertainty originates from the initial phases. For different initial phases, particle aspect of the localized wave packets solutions remains unchanged, while the final behaviour may be drastically affected.

References

[1] R. Rajaraman, *Solitons and Instantons* (North Holland, Elsevier, Amsterdam, 1982).

[2] A. Das, *Integrable Models* (World Scientific, 1989).

[3] G. L. Lamb, Jr., *Elements of Soliton Theory* (John Wiley and Sons, USA, 1980).

[4] P. G. Drazin and R. S. Johnson, *Solitons: an Introduction* (Cambridge University Press, 1989).

[5] D. K. Campbell and M. Peyrard, Phys. D **19**, 165 (1986).

[6] D. K. Campbell and M. Peyrard, Phys. D **18**, 47 (1986).

[7] D. K. Campbell, J. S. Schonfeld, and C. A. Wingate, Physica D **9**, 1 (1983).

[8] M. Peyrard and D. K. Campbell (1983), Physica D **9**, 33 (1983).

[9] R. H. Goodman and R. Haberman, Siam J. Appl. Dyn. Syst. **4**, 1195 (2005).

[10] M. Mohammadi and N. Riazi, Prog. Theor. Phys **126**, 237 (2011).

[11] S. Hoseinmardi and N. Riazi, Int. J. Mod. Phys. A **25**, 3261 (2010).

[12] V. A. Gani and A. E. Kudryavtsev, Phys. Rev. E **60**, 3305 (1999).

[13] C. A. Popov, Wave Motion **42**, 309 (2006)

[14] M. Peyravi, A. Montakhab, N. Riazi, and A. Gharaati, Eur. Phys. J. B **72**, 269 (2009).

[15] T.D. Lee and G.C. Wick, Phys. Rev. D**9** 2291 (1974).

[16] R. Friedberg, T. D. Lee and A. Sirlin Phys. **13**, 2739 (1976).

[17] R. Friedberg and T.D. Lee, Phys. Rev. D**15** 1694 (1977)

[18] J. Werle. Physics Letters. **71B**, 368 (1977).

[19] Werle, J.: Acta Phys. Pol. **B12**, 601 (1981).

[20] S. Coleman, Nucl. Phys. B **262**(2) 263-283 (1985).

[21] T.D. Lee and Y. Pang, Phys. Rep. **221**(5) 251-350 (1992).

[22] N. Riazi, Int. J. Theor. Phys.**50**, 3451 (2011).

[23] R. Abazari and S. Jamshidzadeh, Optik vol.**126** 1970-1975 (2015).

[24] M. Mohammadi, N. Riazi, Prog. Theor. Exp. Phys, 023A03 (2014).

IJAA

COPYRIGHT TRANSFER FORM

I confirm that the enclosed article entitled:

_____

_____

Corresponding Author

Corresponding Author

Signature: _____ Name: _____ Date:_____

Institution: _____ Dept: _____

Street: _____ City:_____ State: _____

Zip/code: _____ Country: _____Country Code:_____

Phone: _____ Fax: _____ Email: _____

IMPORTANT: Papers will not be published unless this form is signed by corresponding author (on behalf of all Authors) and return to the:

IJAA Editorial Office

Damghan University, Damghan, Iran

Iranian Journal of Astronomy and Astrophysics

Postal Code: 36716-41167

Tel-fax: +98-23-35220236

E-mail: ijaa@du.ac.ir

Instruction for Authors

Iranian Journal of Astronomy and Astrophysics peer reviewed international Journal published twice per year, devoted to the publication of original research papers from various field of astronomy and astrophysics. IJAA publishes quality original research papers, comprehensive review articles, short papers in astronomy and astrophysics and its applications in the broadest sense. It aims to disseminate knowledge; provide a learned reference in the field; and establish channels of communication between academic and research experts. Papers should contain results of original research, neither previously published nor under consideration for publication elsewhere. Papers presented at conference which, are only abstracted in the conference proceeding are also welcomed. There are no page charges except color figures. Contribution is open to researchers of all nationalities. All articles indexed and abstracted in (ISC) http://www.isc.gov.ir /

Articles will be published in the following categories:

Review Articles: (up to 25 template-based pages, including tables and figures) critically evaluate recent developments in a specific area of interest to the readership. They are normally invited; authors wishing to submit a review are requested to first contact chief editor.

Papers: (up to 12 template-based pages, including tables and figures) report original research which has not been previously published or submitted, and is not being considered for publication elsewhere. Papers are to be submitted to the Editor in Chief, who evaluates them with the aid of appropriate referees on the basis of scientific quality, originality, and general interest to the readership. The editor may also accept or reject inappropriate manuscripts without consulting referees.

Main Text
The manuscript should include Title, Abstract, Keywords, Introduction (opt.) Results and Discussion (opt.), Experimental (opt.), Acknowledgments (opt.), Conclusions (opt.) and References.

Abstract and Keyword
The abstract should briefly indicate the summary of results discussed in the paper. A list of 3-6 keywords must also be given in this page.

Manuscript Organization
For downloading the article template, please see our website:
http://ijaa.du.ac.ir/data/ijaa/news/tex-sample-97.04.19.zip

Copyright Transfer Agreement
Upon acceptance of an article, the corresponding author will be asked to transfer the signed copyright form (Available in http://research.du.ac.ir/wp-content/uploads/sites/8/2016/11/Copyright.zip) to the publisher on behalf of any and all co-authors. The authors must be warranted that are aware of and agree with all contents of the article and consent to their name appearing on it.

Open Access Policy
This journal provides immediate open access to its content on the principle that making research freely available to the public supports a greater global exchange of knowledge.

Online submission: http://journals.du.ac.ir/
E-mail: ijaa@du.ac.ir

CONTENTS